REVERSIBLE FUEL CELL PERFORMANCE AND DEGRADATION

by

Matthew Aaron Cornachione

A thesis submitted in partial fulfillment
of the requirements for the degree

of

Master of Science

in

Electrical Engineering

MONTANA STATE UNIVERSITY
Bozeman, Montana

April, 2011

© Copyright

by

Matthew Aaron Cornachione

2011

All Rights Reserved

APPROVAL

of a thesis submitted by

Matthew Aaron Cornachione

This thesis has been read by each member of the thesis committee and has been found to be satisfactory regarding content, English usage, format, citations, bibliographic style, and consistency, and is ready for submission to the The Graduate School.

Dr. Steven R. Shaw

Approved for the Department of Electrical and Computer Engineering

Dr. Robert C. Maher

Approved for the The Graduate School

Dr. Carl A. Fox

STATEMENT OF PERMISSION TO USE

In presenting this thesis in partial fulfullment of the requirements for a master's degree at Montana State University, I agree that the Library shall make it available to borrowers under rules of the Library.

If I have indicated my intention to copyright this thesis by including a copyright notice page, copying is allowable only for scholarly purposes, consistent with "fair use" as prescribed in the U.S. Copyright Law. Requests for permission for extended quotation from or reproduction of this thesis in whole or in parts may be granted only by the copyright holder.

Matthew Aaron Cornachione

April, 2011

ACKNOWLEDGEMENTS

I would like to thank my advisor, Dr. Steven Shaw, for granting me the opportunity to work at Montana State University as a graduate research assistant and for providing assistance to many aspects of this work from circuit design to machining parts.

I would also like to thank Dr. Stephen Sofie for providing advice and guidance for testing. His fuel cells expertise was very valuable in advancing the work performed here. In addition, I would like to thank Pete Lindahl and Eric Moog for providing time and advice on various portions of the problem and on electrical engineering in general. Also I would like to thank several members of the mechanical engineering department including Cameron Law and Adam Weisenstein who have helped with many of the fuel cell questions that have arisen.

TABLE OF CONTENTS

1. INTRODUCTION 1

Solid Oxide Fuel Cells 1
Electrolysis 2
Reversible Fuel Cells 4
Thesis Research 6

2. TEST APPARATUS DEVELOPMENT 7

Heating 7
Gas Flow 8
Water Vapor Delivery System 9
Reversible Circuitry 12
Fuel Cells 13
Data Acquisition 17

3. CHARACTERIZATION METHODS 19

IV Sweeps 19
EIS Sweeps 20
SEM Imaging 22
Synthesizing Methods 23

4. COMPARISON OF FUEL CELL AND ELECTROLYSIS PERFORMANCE UNDER VARYING STEAM INPUT 25

Testing Procedure 25
Results 28
IV Data 28
EIS Data 30
SEM Imaging 34
Conclusions 35
Reversible Performance 35
Degradation 38
Oxygen Leakage Concerns 41

TABLE OF CONTENTS – CONTINUED

5. COMPARISON OF DEGRADATION IN FUEL CELL OPERATION TO ELECTROLYSIS OPERATION 44

Test Procedures 44
Results 47
Fuel Cell Test 47
IV Data 48
EIS Data 49
SEM Imaging 52
Electrolysis Cell Test 53
IV Data 53
EIS Data 54
SEM Imaging 55
Conclusions 56
Fuel Cell Test 56
Electrolysis Test 58
Comparison 61

6. DISCUSSION 62

REFERENCES CITED 65

APPENDIX A: Time-Domain Analysis for Electrochemical Impedance Spectroscopy: By Peter Lindahl and Matthew Cornachione 69

LIST OF TABLES

Table Page

4.1 IV parameters 29

4.2 Electrochemical voltage efficiency (EVE) at 1.5A (83mA/cm^2) and 3.0A (166mA/cm^2) at varying steam percentages. 30

4.3 Fuel Cell EIS Results 32

4.4 Electrolyzer EIS Results 32

LIST OF FIGURES

Figure Page

1.1 Illustration of a) fuel cell operating mechanism and b) electrolyzer operating mechanism 3

2.1 Diagram of the test stand illustrating connections to the fuel cell. 8

2.2 Empirical data showing how the molar percentage of water vapor entrained in the hydrogen flow varies with temperature and flow rate. 11

2.3 Diagram of the circuit used in RFC testing featuring parallel OPA 549 op-amps. 13

2.4 Cross sectional view of cell configuration, not to scale. 14

2.5 Cross sectional view of cell configuration with modified platens, not to scale. Platinum leads (not shown) are fed between the two alumina felt layers. 16

3.1 Resistive/capacitive EIS response illustrating R_p, R_s, and f_m 21

3.2 Photograph of an epoxy mold used to cleanly quarter tested fuel cells. 22

4.1 Regenerative IV performance of commercial cell 28

4.2 Plots of the complex impedance of the cell over the frequency range 0.5Hz to 5kHz in fuel cell mode (top) and electrolysis mode (bottom). Each plot compares the impedance with no water input to that at 40 percent steam input. 31

4.3 Complex impedance plots of degraded cell in fuel cell mode (top) and electrolysis mode (bottom). 33

4.4 SEM images of the degraded cell with the cathode on top. Though much of the cell remains intact, prominent cracks were observed in the electrolyte. In addition, some areas show signs of delamination between the electrolyte and electrodes. 35

4.5 Comparison of IV curves with no water vapor at the beginning of the test to the conclusion of the test showing cell degradation. 39

LIST OF FIGURES – CONTINUED

Figure Page

5.1 Initial and final IV performance of a fuel cell operated at 100mA/cm^2 for 100 hours. The cell shows an overall trend toward improved performance. 48

5.2 Hysteresis in the fuel cell IV curve in the electrolysis region. 49

5.3 Initial and final IV performance of a fuel cell operated at -100mA/cm^2 for 100 hours. The cell shows a drop in open circuit voltage and an increase in resistance in the fuel cell region. 50

5.4 Comparison of EIS response at 0 hours, 18 hours, and 100 hours. Initially cell impedance increases substantially. Later the cell shows a significant decrease in ionic polarization resistance, but a small change in series resistance. 51

5.5 Plot of the ionic polarization resistance over the course of the 100 hour test. Except for the spike at the second test point, the ionic polarization resistance shows an overall decrease. 52

5.6 SEM images of the fuel cell operated under a positive current. The cell is oriented with the cathode on the left and anode on the right. The left figure is an undamaged portion of the cell for reference and the right figure shows an instance of delamination between the electrolyte and anode. 53

5.7 EIS response of the electrolysis cell over the course of 100 hours. Initially, the cell impedance increases significantly, but after roughly 60 hours cell impedance decreases. 55

5.8 Plot of the ionic polarization resistance over the course of the 100 hour test. The resistance initially increases dramatically, then remains relatively stable before decreasing 68 hours into the test. 56

5.9 SEM images of the fuel cell operated under negative current. The cell is oriented with the cathode on the left and anode on the right. The left figure is an undamaged portion of the cell for reference and the right figure shows delamination between the electrolyte and cathode. 57

A.1 Phasor representation of the ordinary least squares (OLS) fit voltage and current measurements. 76

ABSTRACT

This thesis presents the development of a test stand to characterize the performance of reversible solid oxide fuel cells. The test stand was used in two different studies to determine the behavior of commercially available solid oxide fuel cells under varying steam percentage input and to compare the degradation incurred during fuel cell operation to that during electrolysis operation. The development of this test stand included construction of a water vapor delivery system using steam entrained in a hydrogen flow and a circuit built from high power op-amps to allow biasing of the fuel cell in both fuel cell and electrolysis mode. The test stand allows the steady state characteristics to be evaluated over a wide voltage range through current/voltage sweeps and the small signal behavior to be examined in-situ through the use of electrochemical impedance spectroscopy. These tests, as well as post-operation field emission scanning electron microscope observation, were used to determine that the cells perform comparably in both modes of operation though the cell resistance tends to be higher in electrolysis mode. It was also found that during extended operation these cells degrade significantly to the point of mechanical failure in electrolysis mode and thus may not be suitable for long term electrolysis operation. The equipment developed here can perform similar tests on newly designed reversible fuel cells to determine whether different materials choices or cell construction provide superior reversible performance and durability.

INTRODUCTION

Solid Oxide Fuel Cells

A fuel cell is a device that converts chemical energy to electrical energy. Fuel cells come in many varieties, including proton exchange membrane (PEM) cells, alkaline fuel cells (AFCs), direct methanol fuel cells (DMFCs) molten carbonate fuel cells (MCFCs), and solid oxide fuel cells (SOFCs). These types of cells have different strengths and weaknesses including relative efficiencies, operating temperatures, available fuel sources, and durability[1]. In addition, certain cells tend to be inherently better than others for a particular application.

The research described in this thesis was performed exclusively with solid oxide fuel cells. These are ceramic based cells designed to operate at high temperatures, typically between 700°C and 1100°C. SOFCs are composed of three primary components: an anode, cathode, and electrolyte. The most common anode material is a combination of nickel and yttria-stabilized zirconia (YSZ). Most cathodes are composed of lanthanum strontium manganite (LSM) or a similar compound. Electrolytes typically consist entirely of YSZ. However, a variety of other materials are used in different applications and the choice for materials that optimize both the performance and cost of solid oxide fuel cells is a subject of continued interest.

SOFCs are of great value for a number of reasons. In particular, these cells have one of the highest efficiencies of any fuel cell, 50-60 percent, and, if used for combined heat and power (CHP) generation can reach efficiencies of up to 80 percent. In addition, SOFCs are capable of utilizing a number of different fuel sources, including H_2, CO, and natural gas, which allows for a wider range of power generation options[2]. Of the possible fuel sources for SOFCs, hydrogen is one of the most environmentally

appealing. If hydrogen is used as a fuel, the only waste gas is water vapor. However, practical SOFC stacks tend to use other fuels due to lower cost.

The SOFCs used in this research were run using H_2 as a fuel and pure O_2, or an O_2 and N_2 mixture simulating air, as the oxidant. The chemical reaction that takes place for this choice of fuel and oxidant is illustrated in Figure 1.1a. In the fuel cell, O_2 is passed across the cathode where it splits into O^{2-} ions and travels through oxygen vacancies in the electrolyte lattice. At the anode, the O^{2-} ions react with an incoming H_2 flow to form water. For this reaction to take place, electrons must travel around the insulating electrolyte. By connecting a load between the cell anode and cathode, a current will begin to flow, producing power.

SOFCs are designed for use in a variety of applications. Because of the high temperature requirement, they are more difficult to use in portable systems and automobiles. However, the high efficiencies of SOFCs make them very well suited to large-scale power generation. Large SOFC stacks are being developed to provide a grid-connected power source. Although the costs are still not comparable to conventional power generation, SOFC technology shows the potential to become economically viable on this scale [1].

Electrolysis

Hydrogen fuel is not easy to come by since terrestrial hydrogen is nearly always found bound to other elements. To use hydrogen as a fuel, it must be separated from another molecule. One common method of generating this hydrogen is through

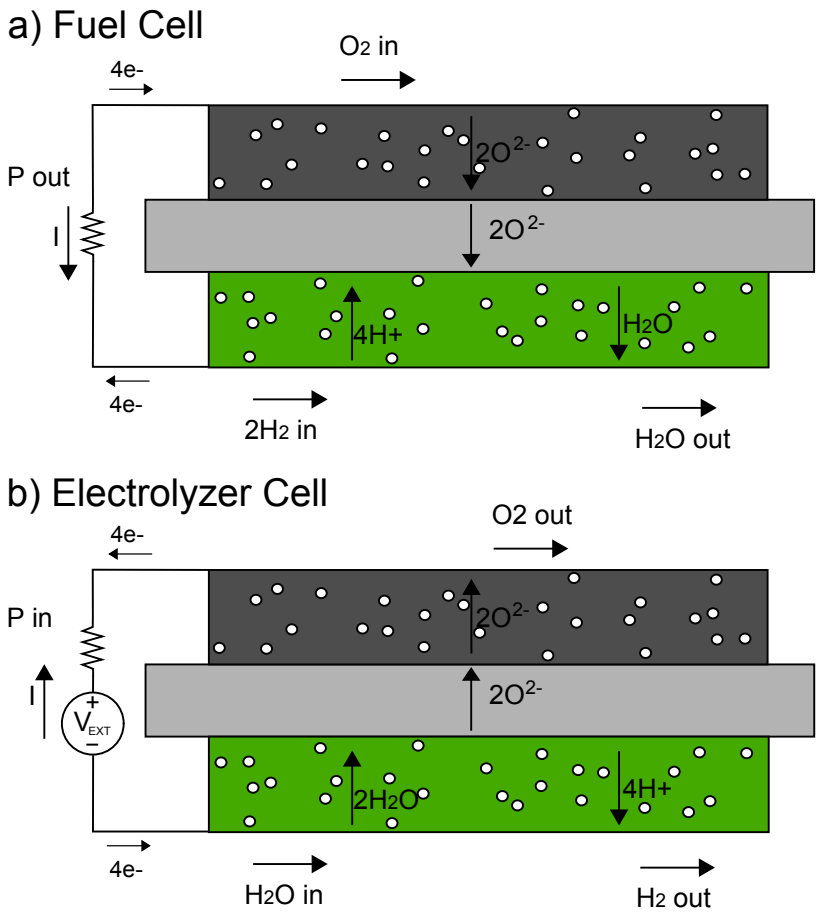

Figure 1.1: Illustration of a) fuel cell operating mechanism and b) electrolyzer operating mechanism

electrolysis of water. Through the reaction $H_2O = H_2 + \frac{1}{2}O_2$ hydrogen and oxygen can be separated. If these gases are stored, they can be later used in an SOFC for power production. Electrolysis efficiency can be very high, ranging between 75 percent and 95 percent.

Electrolysis can be performed through a variety of methods including the use of a fuel cell operating in reverse[3, 4, 5]. This process is illustrated in Figure 1.1b. Water

vapor is passed to the fuel cell anode. Technically the fuel cell anode functions as the electrolysis cell cathode, but for the sake of clarity the side of the cell exposed to hydrogen will be referred to as the anode in both modes of operation in this thesis. At the anode the water splits into its constituents with the reaction

$$H_2O + 2e^- = H_2 + O^{2-} \tag{1.1}$$

Once split, the O^{2-} travels across the electrolyte to the cathode where it recombines to form O_2 and releases electrons which travel through an external circuit to allow the initial reaction to proceed. Note that this requires electrons to travel against the built-in voltage and oxygen ions to travel against the diffusion gradient, hence external power must be supplied to drive this reaction. On the anode side, the additional H_2 can be collected for later use.

Reversible Fuel Cells

A typical SOFC may be designed specifically for use either as a fuel cell or electrolyzer. While it can be possible to use most cells in both modes, the performance and durability tend to be significantly worse during operation in the wrong mode. However, cells can be designed to operate effectively in both modes. A cell intended to be used both as a fuel cell and an electrolyzer is known as a reversible fuel cell (RFC).

In a closed-loop system a reversible fuel cell is called a regenerative fuel cell and can alternatively generate power, and H_2O, from the reactants H_2 and O_2 then use

an external power source to split the H_2O back into H_2 and O_2. Regenerative fuel cell design usually seeks to maximize the round trip efficiency of this reaction [6]. This ability to both produce power and generate hydrogen and oxygen for future use allows RFCs to function much like a rechargeable battery, thus they are typically used as a backup or supplemental power source.

RFCs also have advantages over fuel cells stacks combined with separate electrolyzer stacks since they require less space and tend to allow an overall simpler system. This can be of use in many situations, but is of particular importance in aerospace applications where space and mass is very restricted. RFCs have been designed to serve as long term backup power sources for high-altitude planes, satellites, and in the space shuttle [7, 8, 9, 10]. These cell stacks can also be very effective when coupled with renewable energy sources such as solar power. RFC and solar hybrid systems have the potential to provide uninterrupted power for very long durations [11].

Though RFCs show promise for use in a variety of applications, RFC research and technology lags conventional SOFC technology. This is partly because the materials selection for RFCs is more difficult due to the fact that the anode and cathode must function effectively in two different modes of operation. This necessitates a trade-off between performance and durability and also means that RFC efficiency in either mode of operation tend to be a bit lower than conventional fuel cells or electrolyzers. However, if developed more completely, RFCs show promise to serve as more compact backup power system since a single RFC stack can perform both electrolysis and

produce power. Thus there is interest in further exploring RFC materials options and cell design to improve overall performance.

Thesis Research

The research described in this thesis was performed as part of a NASA grant to examine materials and RFC configuration to create cells capable of improved performance for eventual use as backup power for satellites and spacecraft. The intent is to construct a small reversible cell stack that demonstrates the ability to both produce power and electrolyze water. The cells are intended to be coupled with a solar power input to provide long-term uninterrupted power.

The focus of this thesis is on the development and use of methods to assess the performance of cells to assist in determining the strengths and weaknesses of various materials choices and cell designs. This research included the development a reversible test stand and preliminary analysis of conventional SOFC performance in both fuel cell and electrolysis modes. Determination of cell behavior using current/voltage response and in-situ electrochemical impedance spectroscopy was demonstrated in several reversible cell experiments.

TEST APPARATUS DEVELOPMENT

Regenerative fuel cell testing on SOFCs requires several important capabilities. Like any SOFC, the RFC must be held at high temperature and given a fuel and oxidant input, in this case hydrogen and oxygen gases. However, an RFC also requires the input of water vapor during electrolysis operation. In addition, the electronics used in RFC testing require more consideration than in regular SOFCs because current passes through the cell in both the positive and negative direction. This limits the use of some conventional testing equipment, including power supplies and electronic loads designed for unidirectional current flow.

A schematic of the completed regenerative test stand is shown in Figure 2.1. This illustrates the connections between the various pieces of equipment used in this setup. The design of the apparatus is similar to others in use for regenerative and electrolysis testing [12]. The systems for cell heating and gas flow are based on commercially available equipment and are described first. The newly designed water vapor delivery system and reversible circuitry are outlined next in more detail. The fuel cell installation and data acquisition systems are also discussed.

Heating

Figure 2.1 shows the cell held within an ATS 3210 upright furnace capable of heating up to 1200°C. The furnace temperature is governed by an ATS Temperature Control System, capable of programming temperature ramps. The controller

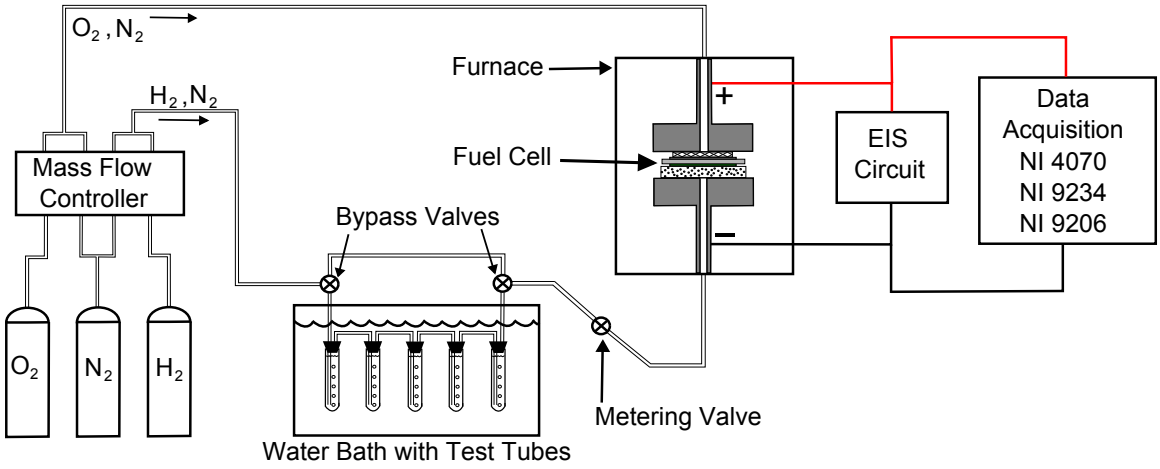

Figure 2.1: Diagram of the test stand illustrating connections to the fuel cell.

measures the temperature with an N-type thermocouple mounted in the oven lining. These readings have been verified using a type K thermocouple with voltage differential measured with an Agilent 34420A nano-volt meter.

Gas Flow

Three types of gases, hydrogen, oxygen, and nitrogen, are used as input to the fuel cell. H_2 can flow to the anode to provide fuel, O_2 can flow to the cathode to provide the oxidant, and N_2 can flow to both sides to purge the lines and serve as an inert gas. The gas flows are governed by MKS Mass-Flo Controllers configured to each gas with a maximum flow of 2000 sccm (standard cubic centimeters per minute) and a minimum flow of 20 sccm. These individual controllers are connected to an MKS 647C Multi Gas Controller which is used to set the desired flow rates on each of

the gases to within ±1% of maximal flow, though typical rates remain within ±0.1% of maximal flow.

Water Vapor Delivery System

Reversible testing of solid oxide fuel cells necessitated the development of equipment to provide water vapor to the cell. Because water is a liquid at room temperature, water vapor flow rates are more difficult to control effectively than are H_2, O_2, and N_2 flows. First, a source of water is heated, then passed through a pipe in a controlled manner to the cell anode to deliver a known amount of water vapor to the cell. This pipe must also be heated in order to prevent condensation which can interrupt the gas flow and potentially lead to the introduction of liquid phase water to the cell. Liquid water can adversely affect performance and potentially damage the cell.

This objective is commonly achieved by bubbling a carrier gas through a tank of heated water [13, 14]. This gas entrains a certain amount of water, delivering a mixture of carrier gas and water vapor to the fuel cell. Since the vapor pressure of water is well known as a function of temperature, the percentage of water in the flow can be well controlled simply by changing the tank water temperature.

For the water vapor delivery system described here, hydrogen is used as the carrier gas and passes through a series of five 100mL test tubes filled with deionized water. The test tubes are submerged in a Cole-Parmer StableTemp 20 liter water bath. The water bath maintains the test tubes at a desired temperature. Adjustment of this

temperature sets the percentage output of water vapor in the hydrogen flow. A bypass pipe allows pure hydrogen to flow straight to the anode without entraining any water vapor.

Gas flow leaves the water bath and travels through a length of 1/4 in. outer diameter stainless steel pipe to the fuel cell. A constant current of 40.0A is run through the pipe to provide resistive heating. As power is dissipated, the pipe temperature remains between 80°C and 100°C, sufficiently hot to prevent significant condensation during the flow passage. This system allows control to a reasonable accuracy, roughly $\pm 5\%$ of total flow, of the water vapor flow to the fuel cell.

A portion of the heated pipe is fitted with a metering valve to mitigate bubble noise on the fuel cell output. It is believed that this noise is caused by pressure fluctuations built up while traveling through the test tubes, leading to substantial flow variation at the output. This can lead to fluctuations of up to 20mV_{pp} (peak to peak) on the fuel cell voltage. With the valve in place, the noise is reduced to less than 1mV_{pp} except at very high water vapor flow rates. The valve is insulated to help maintain a sufficiently high temperature to prevent condensation.

Exact flow percentages were determined experimentally before fuel cell testing commenced. The tests used the apparatus above, but instead of the flow terminating at the fuel cell, it passed through another 100mL test tube filled with drierite. Drierite is a highly absorbent substance capable of removing water vapor from the hydrogen flow. The mass of the tube of drierite was measured before and after a set flow of hydrogen and steam passed through. The change in mass determined the amount of water absorbed, which was converted to moles of water vapor. The moles of hydrogen

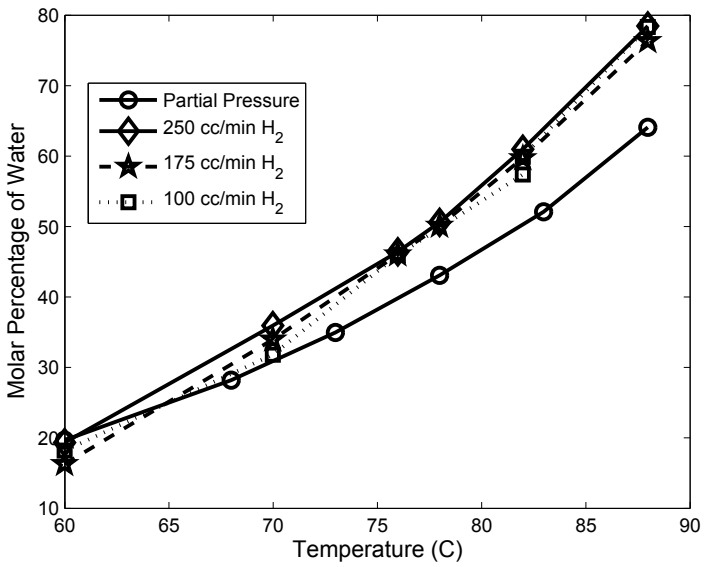

Figure 2.2: Empirical data showing how the molar percentage of water vapor entrained in the hydrogen flow varies with temperature and flow rate.

were determined by noting the hydrogen flow rate set using the MKS controller and the duration of the flow.

The results provided a means to compare the actual percentage of H_2O in the flow to the percentages predicted by the partial pressures of water vapor, shown in Figure 2.2. Actual water percentages tend to be higher than the partial pressure values, likely due to additional free water molecules in the flow of saturated H_2. The percentages do not vary dramatically over the tested range of hydrogen flow rates, thus the output percentage can be considered nearly independent of flow rate and dependent primarily upon water temperature.

Reversible Circuitry

Reversible cells must operate both as a current source and sink. Conventional DC power supplies and electronic loads, often used for fuel cell testing, typically operate only as a current source or sink and thus cannot be placed directly in series with a RFC. In order to effectively test reversible cells, new circuitry was developed to allow voltage control in both modes of cell operation.

The need for bidirectional capability complicates an RFC test circuit design, but a number of methods can provide acceptable performance. The design described in this research uses two high power OPA549T op-amps wired in parallel. The op-amps are able to handle bidirectional current flow and each have a maximum steady current capacity of 8A, allowing for up to 16A total through the fuel cell. These draw power from two LS150-5 5V supplies capable of delivering up to 26A of current. The op-amps dissipate enough power that a heat sink must also attached for cooling. The circuit diagram is illustrated in Figure 2.3.

The fuel cell behavior can be controlled by moderating the voltage at the terminals of the cell. By decreasing the voltage below the cell open circuit voltage, the cell can be run in power production mode. This simulates how the cell behaves when driving a load. However, by increasing the voltage above the open circuit voltage, the cell can run in electrolysis mode. Under those conditions the cell can produce hydrogen and oxygen from any supplied steam.

An Agilent 33220A arbitrary waveform generator (AWG) is used as the voltage input into the circuit. By adjusting this input, the fuel cell terminal voltage can be

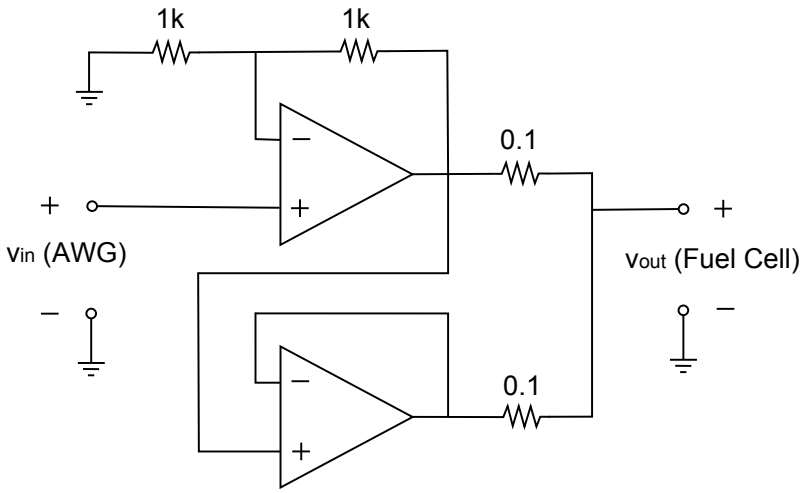

Figure 2.3: Diagram of the circuit used in RFC testing featuring parallel OPA 549 op-amps.

adjusted, thus allowing for fuel cell voltage control. The AWG was used to generate DC signals, voltage ramps, and sinusoidal sweeps. These conditions are of use in fuel cell testing described in chapter 3.

Fuel Cells

Commercially available fuel cells were obtained from H.C. Starck (Indec) to use in testing. These are circular electrolyte supported cells (ESCs) with an electrolyte diameter of 52mm and electrode diameters of 48mm. The electrolyte is approximately 100μm thick and consists of YSZ with 3 percent yttria doping by mole. The cathode is roughly 40μm thick and made from a combination of YSZ with 8% yttria doping and LSM. The anode is also 40μm thick and consists of nickel oxide (NiO) and gadolinium doped ceria (GDC). These cells are designed for use in fuel cell mode, but are also

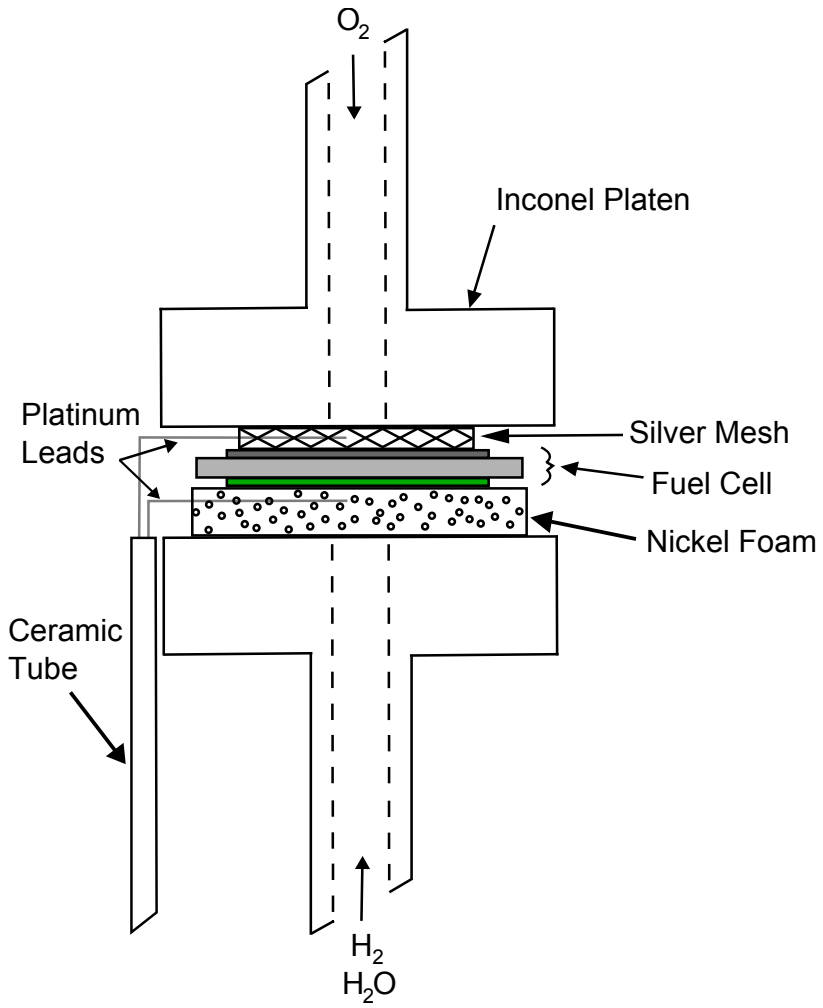

Figure 2.4: Cross sectional view of cell configuration, not to scale.

used in electrolysis mode for the purpose of illustrating the functionality of this test apparatus. The ESC was chosen because the symmetric electrode thicknesses provide similar performance in both modes of operation.

The fuel cells are mounted between two Inconel 600 platens as shown in Figure 2.4. The bottom platen serves as the negative terminal and the top as the positive

terminal. Each platen has a hollow center through which input gas flows. The cell is placed, anode down, onto a piece of nickel foam resting on the bottom platen. The porous foam allows gas to flow from the platen to the cell while serving as a current collector. On the cathode side, a layer of silver mesh is placed between the cell and the top platen. The silver mesh, like the nickel foam, both allows gas to flow and effectively conducts current. Silver paste is used at each interface to reduce contact resistances. The entire structure is placed within the furnace described in the heating section.

For the first experiments, described in chapter 4, the setup was not sealed, meaning that unused gases are vented into the ambient air inside the furnace and, eventually out of the furnace into a fume hood. This open design limits the buildup of potentially damaging impurities, but gives less precise control of the gas on each side of the cell.

Because some of the results displayed anomalous behavior, explained in chapter 4, the fuel cell setup was modified slightly. The intent was to provide some sealing capability without permanently fixing the cell in place. New platens were constructed with two additional features. The new platens have a recess machined into each side that is roughly the thickness of the nickel foam and silver mesh and they have three 0.1 in. diameter holes drilled through them in a symmetric pattern to allow for gas flow. The installation still includes the nickel foam, silver mesh, and silver paste described above, but also uses a ring of compressible alumina felt soaked in alumina slurry around the edge of the platen providing a barrier between the cell anode and the cathode and surrounding atmosphere. The three holes drilled in the

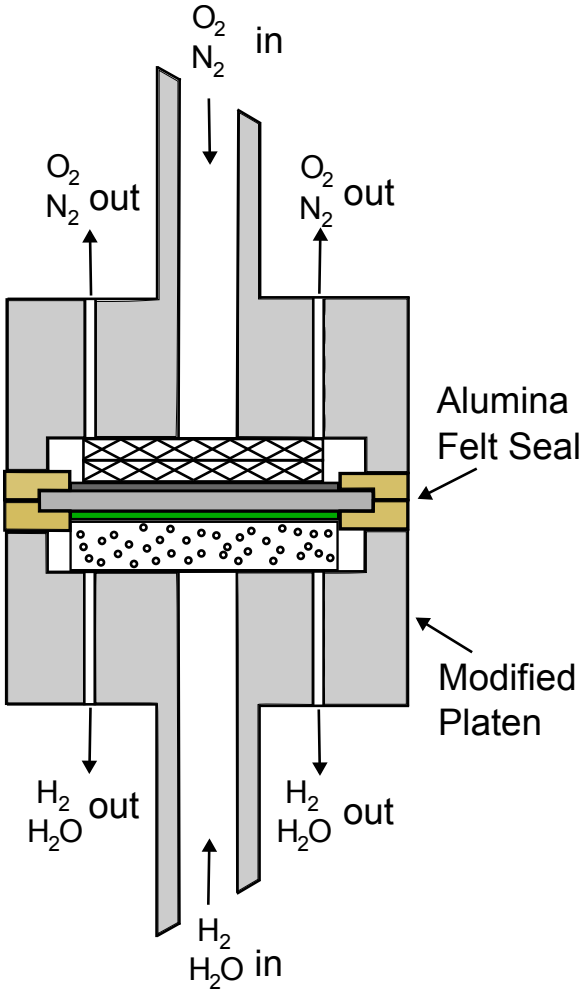

Figure 2.5: Cross sectional view of cell configuration with modified platens, not to scale. Platinum leads (not shown) are fed between the two alumina felt layers.

platen provide an escape route for the gas to prevent pressure build up; however, the path for atmospheric oxygen is tortuous, allowing hydrogen to reduce oxygen at the cell anode. The modified configuration is illustrate in Figure 2.5

Data Acquisition

Cell voltage is measured by wiring two platinum leads the cell, one to the cathode, the other to the anode, also illustrated in Figure 2.4. The cathode wire is woven into the silver mesh while the anode wire slides into a depression formed in the nickel foam, placing the wires in excellent electrical contact with each side of the fuel cell. The wires are then fed out of the oven to an isothermal terminal block where voltage recording equipment is connected. This provides a more precise reading than that obtained from the electrical terminals since the Inconel platens add additional impedance.

An LEM LA 55-P current transducer is placed around the wires to the positive terminal of the cell to measure current. The current output of the transducer, which is 1/1000 of the cell current, runs through a 100Ω resistor to ground. Cell current can then be determined by measuring the voltage across this resistor and multiplying by a scale factor of 10.

These recordings were collected with three different pieces of equipment depending upon the test being performed. First an NI PXI 4070 series DMM connected to an NI computer collects low frequency voltage and current measurements. This is connected to a LabView program to view and save the data. This DMM recorded IV sweeps and other slowly changing phenomena during the experiment described in chapter 4.

Since the AWG driving the fuel cell can perform sine sweeps of the cell, a high frequency data acquisition system was also included. A four-channel NI 9234 24-bit

digitizer with 51.2kHz maximum sample rate monitored current and voltage. The NI 9234 provides excellent noise reduction, but is limited to a maximum sample rate of 25.6kS/s for the two channels. This devices was run through LabView Signal Express and was also used during the experiment described in chapter 4.

While most of the relevant cell behavior takes place at frequencies below roughly 1kHz, it is of interest to be able examine the response at higher frequencies if possible. To allow for this, a 16 differential channel NI 9206 16-bit data acquisition device with a maximum sample rate of 250kS/s aggregate is also used. This allows cell responses of up to roughly 10kHz to be effectively examined. This device is connected by an Ethernet line to a computer which eliminates measurement ground loops and is also run through LabView Signal Express. This device collected data for both IV and EIS sweeps in the second experiment series described in chapter 5.

CHARACTERIZATION METHODS

Fuel cells are complex and imperfectly understood systems. To effectively characterize cell performance, a variety of methods must be used. By comparing results from separate methods, a more complete picture of cell behavior can be formed. This research relied primarily upon three methods: IV sweeps, EIS sweeps, and SEM imaging.

IV Sweeps

IV sweeps involve slowly varying the voltage(V) over a wide range and observing the corresponding changes in current(I). Typical SOFC open circuit voltages (the voltage when no current is drawn from the cell) are near 1.0V. Cell degradation can begin to occur at voltages below approximately 0.2V so IV sweeps performed in this research do not probe voltages below this level. Reversible degradation is less well characterized, but a similar 0.8V from open circuit was used as a guideline meaning that voltages of up to 1.8V were also examined. Typically SOFCs are operated near their point of maximum power output, often near 0.5V, and electrolysis is performed at voltages near 1.3V. Thus the range examined here includes common cell operating points. Data is typically shown in a plot of cell voltage as a function of the current or current density.

EIS Sweeps

One of the most widely used methods for fuel cell characterization is electrochemical impedance spectroscopy (EIS) [15, 16, 17]. This method examines the frequency response of the impedance of the cell at a set operating point, for example, the voltage of maximum power output. This information can be used to help distinguish the mechanisms acting within the cell and provide a more detailed look at cell behavior than IV sweeps. The observed response represents the average of all mechanisms in the cell, thus it is up to the individual researcher to try to interpret the meaning of this information. Unfortunately, there is no standard method of interpretation, though there are still a number of conventional interpretations.

To perform EIS in this thesis, a small amplitude sine wave, approximately 30mV, was applied to the cell at the chosen operating point. The amplitude must be small to ensure that the cell stays within an approximately linear range of operation [15]. The frequency of the sine wave is swept over the range of interest, which for this research was chosen as 0.1Hz and 10kHz. The cell voltage and corresponding current are recorded over the frequency range. The data is then analyzed in the time-domain using a linear least-squares fit approach detailed in the appendix.

The complex impedance is reported on a Nyquist plot which shows the real versus imaginary impedance as a parametric function of frequency. This plot can be fitted to a circuit model with elements corresponding to various fuel cell components. A large variety of different models have been suggested by different researchers [18]. However, the conclusions drawn from this approach are highly dependent upon the

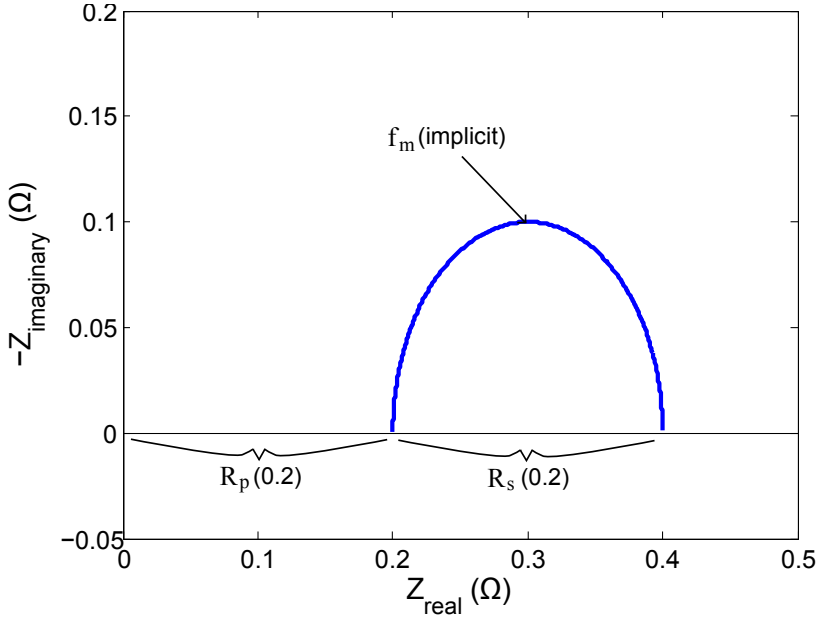

Figure 3.1: Resistive/capacitive EIS response illustrating R_p, R_s, and f_m

specific model chosen and in reality no definitive fuel cell circuit model has been developed. Alternatively, parameters of the Nyquist plot, including the ionic polarization resistance, R_p, series resistance, R_s, and frequency of maximal imaginary response, f_m, can be identified. These parameters are illustrated on an example plot in Figure 3.1. The series resistance corresponds roughly to the sum of the electrode resistances while the ionic polarization resistance corresponds roughly to the resistance of the electrolyte to oxygen ion transport. The sum of the two gives a measure of the DC resistance. The frequency of maximal response suggests the rate at which the electrode interactions take place and, along with the series resistance, can give an estimate of the total electrode capacitance.

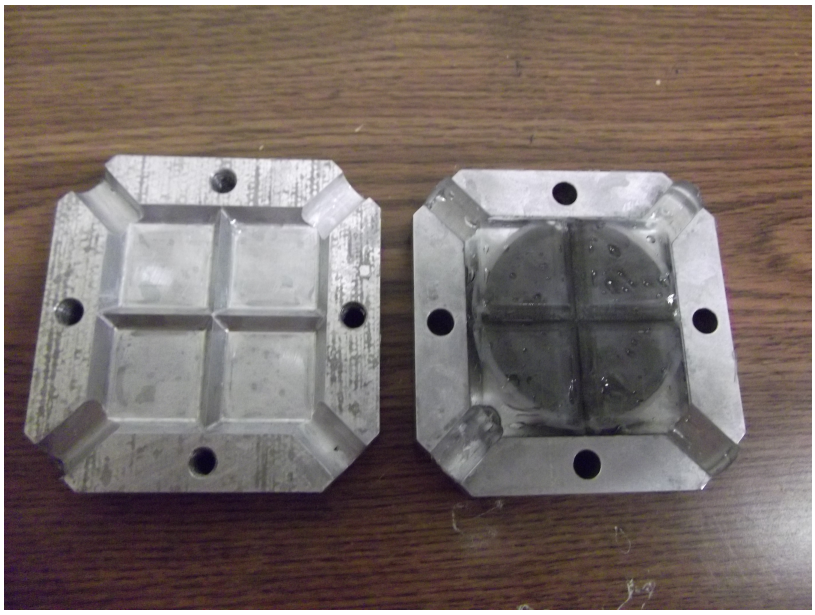

Figure 3.2: Photograph of an epoxy mold used to cleanly quarter tested fuel cells.

SEM Imaging

The third analysis technique is applied after the conclusion of the test. Field emission scanning electron microscope (SEM) imaging allows the visual assessment of cell microstructure after performance testing. This can be used to determine whether any mechanical cell degradation has occurred and, if so, which areas of the cell are most affected. The method requires some subjective interpretation, but can be an invaluable tool in connecting electrical performance variations to physical cell damage.

Before reliable imaging can be performed, the cell must be properly prepared. Once the oven has cooled in an inert gas atmosphere to room temperature, the cell is removed from the test stand and placed into a mold shown in Figure 3.2. This is

designed to quarter the cell without creating any damage beyond that endured during testing by concentrating stress along two lines. To mount the cell, the mold is first sprayed with a silicone release agent. Next the cell is placed into the mold, which is bolted closed. Then a slow curing epoxy is poured around the cell and allowed to set for a full week. Finally, the mold is opened and the cell is removed and broken along the designed weak points. Before imaging, the cell surface is polished to a smooth finish.

Polished cells are sputter coated with iridium and viewed under the SEM. The SEM scan can locate delamination between electrodes and electrolyte, pitting, coarsening, and other types of damage, if any damage has been done. Several images of each cell cross section are saved for later review including close up images of interesting areas. This technique can be limited because the area scanned is only a small portion of the total cell. Nevertheless, the damage observed on the scans provides some idea of the microstructural changes to the cell.

Synthesizing Methods

Information from each of the three methods can be integrated to form an overall idea of cell behavior. The IV data provides information on the power output in fuel cell mode and the power required in electrolysis mode. This can determine the relative efficiency of the cell under difference conditions and can be very relevant to practical cell operation. EIS data gives information only at one or two points of cell operation on the IV curve, but shows more details about the components of the cell. Shifts in

IV performance can be correlated to changes in either the series or ionic polarization resistance to suggest where the changes are taking place within the cell. If these changes lead to cell degradation and mechanical failure, they will often be observed in the SEM scans. This can confirm hypothesis on likely cell weak spots or reveal other damage that must be considered. The three methods together can pinpoint where the cells are most likely to fail and determine the effect of failure on electrical characteristics. This allows future research to focus on improving the proper areas of the cell to increase overall performance.

COMPARISON OF FUEL CELL AND ELECTROLYSIS PERFORMANCE UNDER VARYING STEAM INPUT

One of the immediate uses of the test stand is apparent in the comparison of the performance of the fuel cell under power production operation to electrolysis operation. This test examined the EIS and IV response of a cell under water input percentages varying from 0% water input to 50% water input to the anode with the remainder of the gas pure H_2. This information can be used to suggest the conditions under which the cell should be operated for maximal performance in fuel cell and electrolysis mode.

Testing Procedure

To begin the test, the oven was turned on and heated to 500°C at a rate of 3°C per minute. Once the oven reached 500°C, nitrogen flow was turned on to the anode side at 80 sccm and oxygen flow was turned on to the cathode at 30 sccm. Under these gas flows, the oven continued to heat up at 3°C per minute until it reached the operating temperature of 750°C. At this temperature the oxygen flow rate to the cathode was increased to 100 sccm, the nitrogen flow rate was turned off, and hydrogen flow was gradually increased to the anode over 20 minutes until it reached a final flow rate of 200 sccm. The cell was then allowed to rest at open circuit conditions with no external voltage applied for roughly 12 hours to ensure anode reduction of NiO and full cell activation.

Once the cell achieved activation, several IV sweeps were run to verify that the cell was functioning normally. For these sweeps, the voltage was varied from approximately 0.2V to 1.8V, as explained in chapter 3, at a constant rate over 50s. Curves were obtained in both directions, that is starting at 0.2V and increasing to 1.8V and starting at 1.8V and decreasing to 0.2V so some slight hysteresis effects could be observed, particularly in electrolysis operation. However, since the hysteresis was small, the reported curves are those starting at 0.2V and increasing to 1.8V.

After the IV curves were obtained, the cell voltage was set to 0.6V, well into the ohmic region of operation. Here, sine sweeps were performed to obtain data for use in EIS analysis. These sweeps had amplitudes of approximately 30mV, which corresponded to roughly 200mA, and covered the frequency range 0.5Hz to 5kHz. This range was covered in 4 sweeps, each lasting over one decade of frequency. The lowest frequency sweep, from 0.5Hz to 5Hz, ran for 100s, while each successive sweep lasted for a decade less in time down to 0.1s for the highest frequency sweep. By splitting the sweep into sections reliable data can be obtained at each frequency without requiring an extremely large data set size. However, this method can have the disadvantage of introducing small discontinuities due to end effects in the Nyquist plot between each sweep.

Once the EIS sweeps were completed at 0.6V, the cell voltage was increased to 1.4V and the process was repeated. The 1.4V bias point was within the ohmic region of the cell in electrolysis mode. These two bias points are both 0.4V from 1V, which is the typical open circuit voltage of the cell, and thus provide a good comparison of fuel cell and electrolyzer response.

After baseline cell performance was determined with no steam input, the hydrogen flow was redirected through the water delivery system. The water bath temperature was increased to alter the percentage steam in the hydrogen flow. Target percentages were 20, 30, 40, and 50 percent which were empirically found to correspond to water temperatures of 61, 67, 73, 78°C (see Figure 2.2). During the entire test, the hydrogen flow was held at a constant 200 sccm, thus the total flow to the anode increased with water temperature.

At each change in percentage water, the series of tests described above was repeated. First two IV sweeps from 0.2V to 1.8V were run to examine the shape of the curve under different water conditions. Next, the cell voltage was held at 0.6V while EIS sweeps were taken in the power production mode. Finally, the voltage was held at 1.4V and EIS sweeps were obtained in electrolysis mode.

Once the tests were completed, the hydrogen flow was redirected so that no more water vapor was entrained in the flow. A final series of tests was run to determine ending cell performance. Then the hydrogen and oxygen flows were turned off while nitrogen flow to the anode side was turned up to 200 sccm. The oven was then turned off and allowed to cool under inert gas flow. Once the temperature dropped below 500°C, the nitrogen flow was also turned off for the remainder of the cooling process.

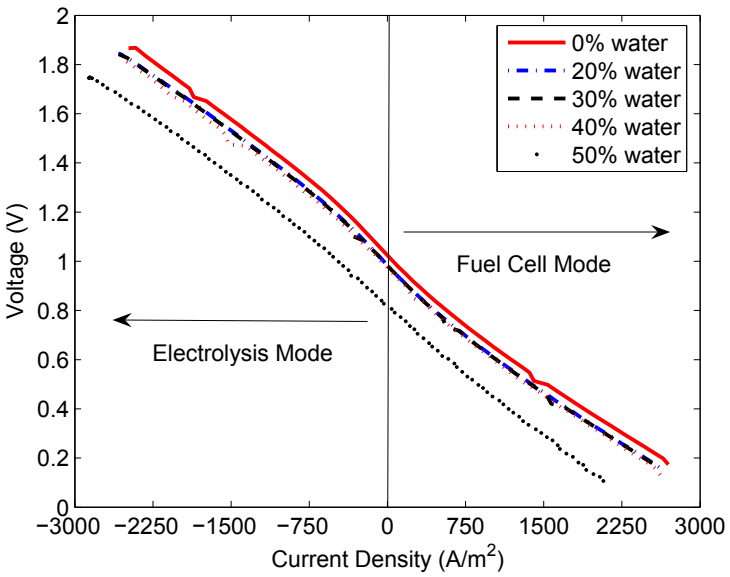

Figure 4.1: Regenerative IV performance of commercial cell

Results

IV Data

Figure 4.1 shows the full IV curves obtained at varying water percentages. The cell curve shifts down as water input increases from 0 percent to 20 percent, but increasing the inlet water percentage from 20 percent to 40 percent has virtually no further effect on cell behavior. This suggests that under these conditions, the cell is essentially saturated at 20% inlet water. The large change at the 50 percent water point is attributed to degradation of the cell described in the degradation section.

Values of the open circuit voltage (OCV), fuel cell ohmic resistance (R_{FC}), and electrolysis cell ohmic resistance (R_E) for each input are listed in Table 4.1. The

Steam Percentage	OCV (V)	R_{FC} (Ω cm^2)	R_E (Ω cm^2)
0	1.026	2.72	3.18
20	0.985	2.84	3.02
30	0.984	2.89	3.06
40	0.976	2.82	3.10
50	0.819	3.16	3.07

Table 4.1: IV parameters

values for R_{FC} and R_E were determined by fitting a line to the ohmic regions of the cells, roughly 0.2 to 0.6V in fuel cell mode and 1.4 to 1.8V in electrolysis mode. This information shows that the open circuit voltage decreases as percent steam increases, which is consistent with expectations. It also shows that fuel cell resistance tends to increase slightly as water percentage increases while electrolysis resistance tends to decrease slightly.

The electrochemical voltage efficiency (EVE) of the cell under different water percentages is also shown for two operating points, I = 3A and I = 1.5A in Table 4.2. The EVE is determined by the ratio of cell power output (P_{FC}) to electrolyzer power input (P_{EL}) [6]:

$$EVE = \frac{P_{FC}}{P_{EL}} \tag{4.1}$$

The EVE is commonly evaluated at identical current densities for fuel cell and electrolyzer modes. This essentially provides a measure of the round trip efficiency of the cell operated under a net zero hydrogen production/depletion. For this cell, the EVE is approximately 53 percent under a moderate current and decreases as current increases to approximately 28 percent near the maximum fuel cell power output

Steam Percentage	EVE (%) at 1.5A	EVE (%) at 3.0A
0	52.2	28.7
20	52.4	27.3
30	53.4	27.1
40	53.0	27.2
50	44.2	16.9

Table 4.2: Electrochemical voltage efficiency (EVE) at 1.5A (83mA/cm^2) and 3.0A (166mA/cm^2) at varying steam percentages.

current. The EVE is not dramatically affected by the change in water percentage in these ranges. However, the EVE does drop significantly at the 50 percent water input operating point which is consistent with cell degradation.

EIS Data

EIS data for both fuel cell and electrolysis operation can be seen in Figure 4.2. These plots compare the complex impedance of the cell with no water input to the cell with 40% water in the input flow. Data for all the sweeps collected is shown in Table 4.3 for fuel cell mode and Table 4.4 for electrolysis. This includes the ionic polarization resistance, R_p, where the resistance is purely real near 500Hz, the estimated DC resistance, R_{DC}, where the resistance is again purely real at zero frequency, and the ohmic resistance $R_s = R_{DC}$-R_p. In addition, f_m, the frequency of maximal imaginary resistance, is given to show differences in frequency response over the range of water input.

Figure 4.2 and Table 4.3 show that the response in the forward quadrant does not change substantially with a change in input water. It appears that at this bias point, the resistance increases roughly 4 percent, but the characteristic shape changes

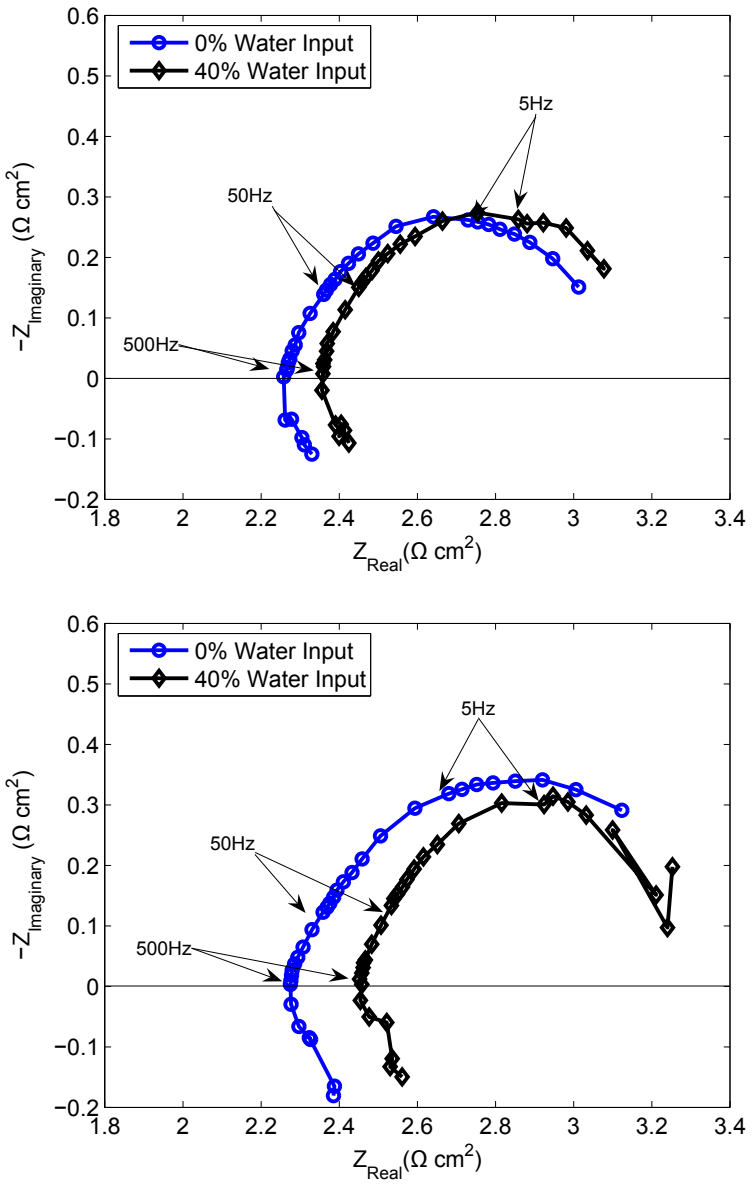

Figure 4.2: Plots of the complex impedance of the cell over the frequency range 0.5Hz to 5kHz in fuel cell mode (top) and electrolysis mode (bottom). Each plot compares the impedance with no water input to that at 40 percent steam input.

Water Vapor (%)	R_p (Ω cm^2)	R_{DC} (Ω cm^2)	R_s (Ω cm^2)	f_m (Hz)
0 (initial)	2.27	3.13	0.86	7.2
20	2.38	3.18	0.80	8.2
40	2.36	3.21	0.85	7.2
50	2.40	3.57	1.17	6.8
0 (final)	2.08	N/A	N/A	N/A

Table 4.3: Fuel Cell EIS Results

Water Vapor (%)	R_p (Ω cm^2)	R_{DC} (Ω cm^2)	R_s (Ω cm^2)	f_m (Hz)
0 (initial)	2.28	3.45	1.17	1.9
20	2.46	3.32	0.86	3.5
30	2.48	3.40	0.92	3.6
40	2.46	3.35	0.89	4.1
50	2.33	3.01	0.68	4.2
0 (final)	1.94	2.94	1.00	2.9

Table 4.4: Electrolyzer EIS Results

little. The curves both reach a maximum at almost exactly the same f_m, just over 7Hz. This suggests that the mechanism of transport in fuel cell mode is unchanged by the addition of water to the anode.

This EIS data is also useful for characterizing the degradation of the cell. Figure 4.3 shows the fuel cell and electrolysis modes for the cell after degradation. These curves were obtained at 0.4V and 1.4V bias points, different from the standard bias points since due to degradation 0.6V was barely in the ohmic region of the cell and no longer a satisfactory bias point. The curves here were obtained after 17 hours of cell recovery with no water input. Comparing Figure 4.3 to Figure 4.2 reveals that the response in fuel cell mode has changed dramatically. The cell shows a very different low frequency response from previous behavior. However, the cell appears to still be

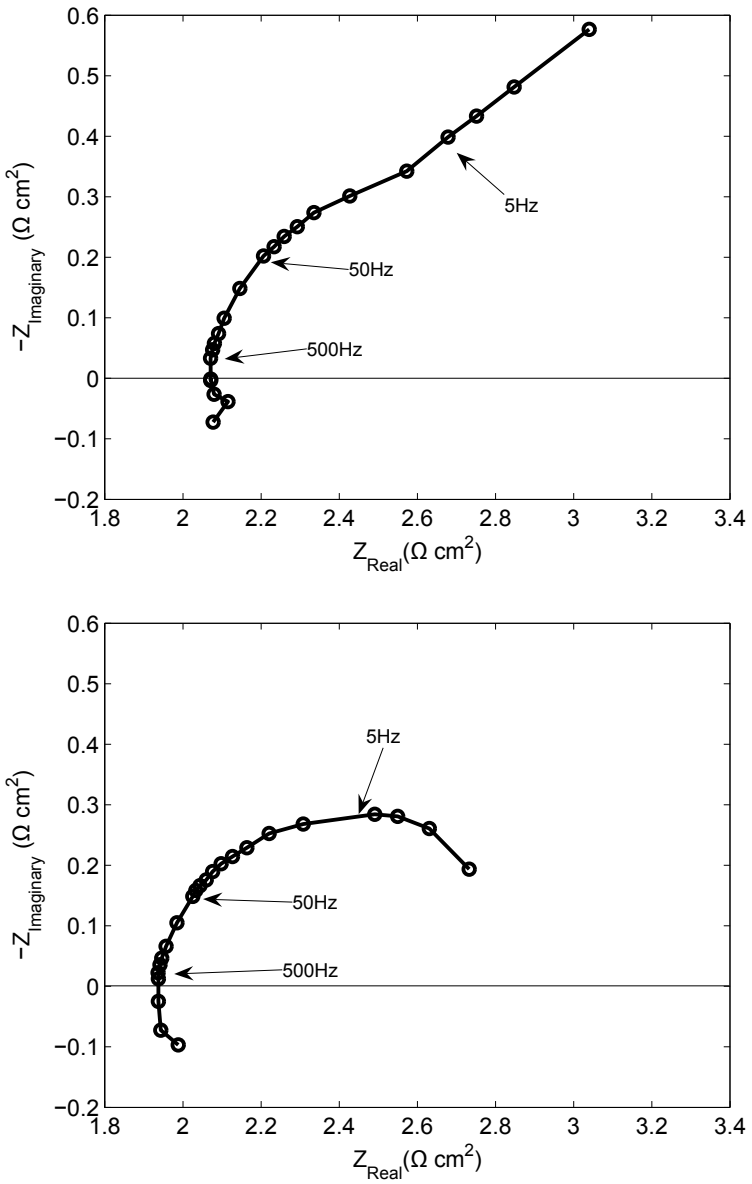

Figure 4.3: Complex impedance plots of degraded cell in fuel cell mode (top) and electrolysis mode (bottom).

functioning normally in electrolysis mode with a slightly lower resistance suggesting improved electrolysis performance.

SEM Imaging

This cell was visibly damaged at the end of the test procedure. It was filled with cracks and fractured into multiple pieces upon removal from the oven. This damage prevented the use of the standard mold described previously. Instead the largest cell fragment was mounted upright with a paper clip in a cylindrical mold. The same epoxy and sample preparation procedures were used with the alternative mold.

The SEM imaging showed that the cell microstructure was mostly intact despite the clear macro level damage. The cell anode and cathode do not display any obvious signs of pitting or substantial coarsening. Some small cracks can be observed between the electrolyte and electrodes, particularly the cathode, marking the beginnings of delamination. However, the most significant damage occurred within the electrolyte. Multiple cracks were observed through the electrolyte as shown in Figure 4.4. Cracks are oriented both parallel and perpendicular to the electrolyte plane. The most severe crack crosses entirely through the electrolyte, but does not pass into the anode, suggesting that the damage originates in the electrolyte. Similar damage has not been observed in related literature and the source of these cracks remains uncertain.

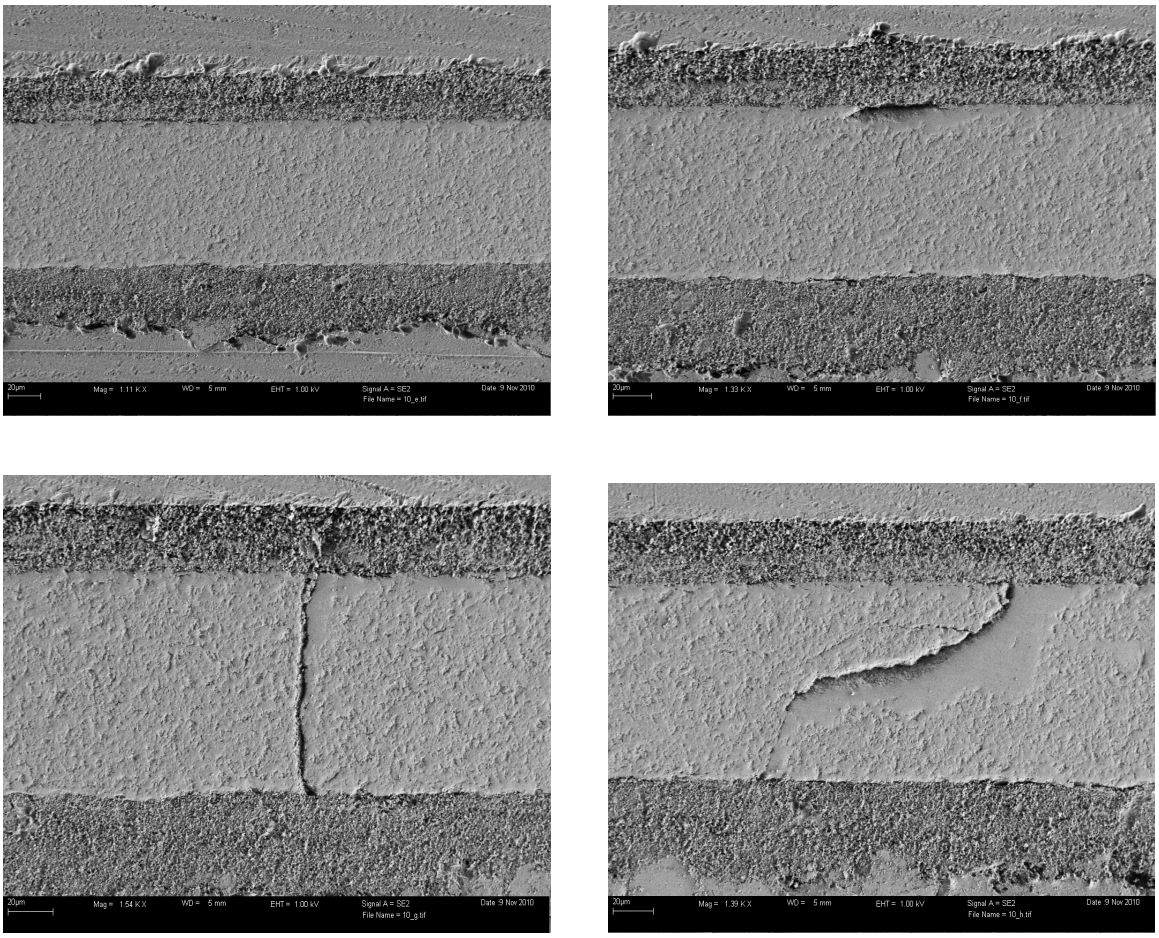

Figure 4.4: SEM images of the degraded cell with the cathode on top. Though much of the cell remains intact, prominent cracks were observed in the electrolyte. In addition, some areas show signs of delamination between the electrolyte and electrodes.

Conclusions

Reversible Performance

From the test results it is clear that although the fuel cells used were designed for use in power production mode, they are capable of functioning as electrolyzers.

Indeed, the performance in both modes of operation is comparable, with resistance tending to be roughly 10 percent higher in electrolysis mode as seen from both IV and EIS data. This ratio changes slightly with changes in water percentage, but remains relatively constant.

Given that this cell can be used as a reversible fuel cell, it is of interest to determine what effect the change in water percentage has on performance. The changes in fuel cell operation were not very dramatic until cell degradation occurred. The IV data suggests a slight increase in overall resistance, accompanied by a decrease in open circuit voltage. From the EIS data on Figure 4.2, it is apparent that the ionic polarization resistance tends to increase as water percentage increases, though series resistance stays nearly constant. Some of this can be attributed to a change in operating point, since equal voltages do not mean equal currents as seen in Figure 4.1. Since ionic polarization resistance is associated with electrolyte impedance, it appears that the ionic resistance of the electrolyte increases as water percentage increases. An increased percentage of water at the anode means that the oxygen content at the anode will be high, thus the concentration gradient of oxygen is decreased, slightly lowering oxygen transport rates. This also accounts for the observed decrease in open circuit voltage.

Observed changes are more significant in electrolysis operation. From the IV analysis, the resistance appears to decrease very slightly, less that 5 percent, as water percentage changes, but EIS analysis reveals that the change is more substantial. The DC resistance on the EIS curves in Figure 4.2 (bottom) is comparable, which agrees with the IV data, but the underlying change in response is more dramatic. As

water percentage increases, the ionic polarization resistance increases substantially, the series resistance decreases, and the frequency of maximal response increases. The latter two points suggest that the process at the cell electrode is happening more easily since the resistance has decreased and it is excited most at a higher frequency. This is consistent with the expectation that with more available fuel, water vapor, the chemical processes happen more readily. The source of the increase in the ionic polarization resistance is uncertain though it is likely at least partly attributable to the higher currents seen at the operating point with more water available. The current transfers oxygen ions across the electrolyte, changing the relative percentages at anode and cathode such that the concentration gradient increases making further oxygen transfer more difficult.

These observations suggest the conditions under which the cell should be operated for maximum performance output. In fuel cell mode, the resistance is the lowest with no water input and thus the corresponding power output is the highest. However, in electrolysis mode the resistance is lowest with high water input. This is consistent with observations in other experiments [19], but it means that for maximal performance, the water input must vary depending on which mode the cell is operated in.

The EVE values listed in Table 4.2 suggest that the percentage water does not have a large effect on round trip performance in the range observed. The best EVE at 3A is 28.7% with 0% steam input while the best EVE at 1.5A is 53.4% at 30% steam. However, if the cell was operated in ideal conditions, such that in fuel cell mode the cell had no steam input and in electrolysis mode the cell had 40% steam input the

EVE can be increased to 30.8% at 3A and 59.5% at 1.5A. Note that even this ideal cell EVE is low compared to leading reversible fuel cells[6], but that is mostly due to the inherent inefficiency of electrolyte supported cells. The thick electrolyte increases the ionic resistance substantially, lowering the power output and increasing the required power input at a given voltage.

Degradation

Each of the three characterization methods shows strong evidence that the cell was degraded during operation under 50% water vapor input. The IV data perhaps is the easiest to interpret. From Figure 4.1, it is clear that the cell performance changes very dramatically once 50% water input is reached though the performance varies little over the rest of the range examined. This behavior persists even when the cell is returned to 0% water vapor input as shown in Figure 4.5. Instead of returning to the initial behavior, the cell performance does not improve, suggesting irreversible cell degradation.

This observation is corroborated by the EIS data collected at the end of the experiment. The fuel cell mode plot in Figure 4.3 shows a dramatic change in characteristics with the degradation. The ionic polarization resistance has actually dropped, though this is likely due to the formation of cracks in the electrolyte, allowing easier oxygen passage. However, the DC resistance is impossible to determine from this plot. Instead of a decrease in imaginary impedance magnitude as seen in a properly operating cell, the imaginary impedance continues to be driven farther from the real axis at low frequencies. This suggests that the fuel cell processes have changed dra-

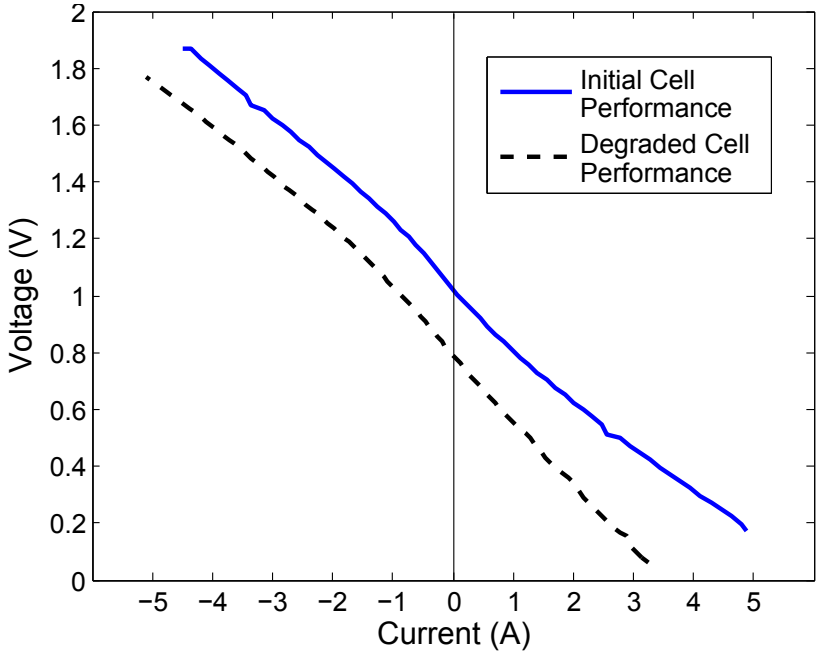

Figure 4.5: Comparison of IV curves with no water vapor at the beginning of the test to the conclusion of the test showing cell degradation.

matically and respond very slowly to changes in voltage. It does appears that the high frequency response is similar to that seen in Figure 4.2, suggesting that primary mechanism of oxygen transport is still taking place. This is consistent with the IV curves which show that there is still limited operation in fuel cell mode.

The cell does not display the same degree of deviation in electrolysis mode. A similar decrease in ionic polarization resistance is observed, but otherwise the curve appears very similar to previous curves. Indeed, compared to the initial curve without water the cell has a lower series resistance and a higher peak frequency. This shows all the signs of improved electrolysis performance, though the series resistance remains higher than that seen with water supplied. This improvement is potentially due to

oxygen leakage through the cracks in the electrolyte. Such leakage would tend to reduce the concentration gradient of oxygen across the electrolyte and reduce the built-in voltage across the cell. Both effects would tend to make further oxygen transport easier, possibly accounting for the observed decrease in impedance.

However, the decrease in impedance does not necessarily correspond to improved electrolysis performance. It is possible for leaking oxygen to bind the carrier hydrogen and form additional steam at the cell anode. This additional steam could take part in electrolysis and account for a portion of the observed current. However, any current due to this steam has a zero net contribution to hydrogen output since the electrolyzed hydrogen was free initially. For a complete determination of cell performance, output hydrogen flow rates would need to be measured and compared to input hydrogen flow rates, which is beyond the capabilities of this test stand.

The precise mechanism of degradation cannot be determined with certainty from this data, but there are several plausible mechanisms. It was observed that under 50% steam input the cell voltage displayed periodic large dips consistent with very high steam input for a short period of time. It appears that while the average water vapor flow rate was near 50% there were period spikes of very high water content. This may be due to moderate pressure buildups and releases within the system, likely behind the metering valve, which has the smallest inner diameter. This may be due to condensation of water within the valve, which as a larger element has lower resistance and tends to remain cooler than the rest of the pipe. If this is the case, more carefully controlled heating should prevent these spikes in future tests.

If condensation was occurring anywhere within the line, then liquid phase water may have been pumped to the cell anode. Even if the water was not in liquid phase, the observed spikes correspond to a higher pressure incident flow for brief impulses. In either case, the water flow may have caused sufficient physical stress on the electrolyte to create these cracks. High flows of water, with a relatively high specific heat capacity, could also have possibly cooled the cell rapidly enough at the anode to create thermal stress within the cell capable of causing the observed cracks. Alternatively, oxygen could have built up within the electrolyte, increasing pressure until internal cracks began to form [20]. In any case, the observed electrolyte damage would have been sufficient to reduce the structural integrity of the cell, leading to the observed macro-scale fragmentation. Since the electrolyte is the structural support of the cell, it would have suffered the most damage, which is consistent with the SEM images suggesting that the cracks originate within the electrolyte.

Oxygen Leakage Concerns

Unexpected behavior was observed for the cell with no steam supplied. Here the cell still demonstrates the ability to conduct a substantial negative current as evidenced by the IV data in Figure 4.1. Indeed it appears that cell performance changes little with or without steam applied. This is counter to theoretical expectations for ideally a reverse current can only occur when oxygen, split from water, travels across the electrolyte. This process requires steam, or at least oxygen, to be present at the cell anode. It should not be possible for the cell to conduct a significant negative current without steam input.

This issue is believed to be due in part to the nature of the experimental setup. While the tendency is to assume that the cell anode is exposed only to the gas that is explicitly pumped in, the effect of the surroundings must also be considered. Since this experiment lacks a seal around the cell, both ambient oxygen and inlet oxygen from the cathode are able to mix with hydrogen at the cell anode in an uncontrolled manner. The evidence from these IV curves suggests that this allows a certain percentage of steam to form at the anode. This allows the passage of reverse current even without the intentional addition of water vapor.

To further support this hypothesis, the theoretical and experimental open circuit voltages are compared. According to the Nernst equation, the open circuit voltage is determined by [21]:

$$E = E_o + \frac{RT}{nF} ln \left(\frac{(p_{H_2})(p_{O_2})^{\frac{1}{2}}}{p_{H_2O}} \right) \tag{4.2}$$

where

$$E_o = 1.253 - 2.4516 \times 10^{-4} T \tag{4.3}$$

In these equations, n is the number of electrons in each atom of the fuel (n=2 for H_2 and H_2O), F is Faraday's constant = 96485.34 $Cmol^{-1}$, R is the universal gas constant = 8.314 $JK^{-1}mol^{-1}$, T is the temperature in Kelvin, and p_α is equal to the partial pressure of gas α for H_2, O_2, and H_2O.

For the experiment described above, the temperature is T = 1023K and the partial pressure of oxygen, p_{O_2}, is assumed to be approximately 1 (almost all gas at the cathode is oxygen). For a fuel input consisting of mostly (99%) hydrogen, the

open circuit potential should be 1.205V. However, measurements show an open circuit potential of 1.026V, 15 percent lower than expected, with only hydrogen supplied to the cell. If instead there is some mixing of hydrogen and oxygen at the anode, calculations show that a mixture of 36.8% water vapor and 63.2% hydrogen at the same test conditions would generate the observed open circuit potential of 1.026V. This suggests that some portion of the hydrogen inflow is reacting with ambient oxygen to give a relatively high effective steam percentage at the cell anode. This would be more than enough steam to support the observed negative currents.

Oxygen leakage also explains the lack of a significant change in IV slope when input water percentage was increased. Although more water enters the cell, the percentage change remains relatively small. Since the rates of oxygen infiltration and water generation are undetermined, the exact water percentages cannot be reliably predicted. However, from the change in open circuit voltage, an estimate of the effective water percentages can be obtained. At 20% input, the OCV suggests that there is actually 59.8% water at the anode. At 30% input there is 60.3% water and at 40% input there is 64.2% water. Though the effective percentage increases with input water increase, the change is relatively small.

These observations have lead to efforts to improve cell sealing without causing damage to the cell during operation or removal. The development of the new platens described in chapter 2 was based upon these observations. The new platens were used as fuel cell interconnects in the second series of experiments.

COMPARISON OF DEGRADATION IN FUEL CELL OPERATION TO ELECTROLYSIS OPERATION

The durability of cells under long periods of testing is very important for practical cell operation. Cell longevity tends to vary depending on how they are designed and whether they are used in fuel cell mode or electrolysis mode. The test described in this section involved two experiments. First, a fuel cell was held under a mild current density for 100 hours and initial and final operating points were compared to assess overall degradation. Second, a new but identical fuel cell was held under the same current density in electrolysis mode for 100 hours to observe degradation. IV sweeps were performed at the beginning and ending of each test while EIS sweeps were performed twice daily during each 100 hour test.

Test Procedures

Both the fuel cell and electrolysis cell test followed the same standard procedure, similar to that in previous tests but with some slight modifications. The cells were placed in the test stand described above with the modified platen setup shown in Figure 2.5. The new anode platen has a recess for the nickel foam to rest in. Alumina felt, soaked in an alumina slurry to help reduce porosity, is placed in a ring around the edge of the platen to serve as a seal for the cell anode. The cell is pushed into the compressible felt and rests upon the nickel foam. Another layer of felt is placed above the cell to serve as a seal for the cathode side of the cell. Two layers of silver

mesh are now used to ensure that the cell cathode is in contact with the top platen. When the seal functions as intended, gas will enter through the center hole of the platen and leave through the three relief holes. The ratio of each relief hole length to diameter is roughly 10, which lowers the amount of extraneous gas entering the cell compared to the previous design.

Once mounted, the cells are heated up at the same rate of 3°C per minute up to 500°C. At this time flows are turned on to provide 20 sccm of oxygen and 20 sccm of nitrogen to the cathode and 80 sccm of nitrogen to the anode. The cell is further heated until the temperature increases to 800°C, the final operating point. Once the cell has reached 800°C, gas flows are increased to 50 sccm of oxygen and 200 sccm of nitrogen to the cathode and 200 sccm of hydrogen to the anode. The cell is then held at open circuit for approximately 12 hours to ensure activation. The primary changes from the procedure in chapter 4 are the increased temperature and the cathode flow of an oxygen/nitrogen mixture simulating air rather than pure oxygen. These changes were chosen to compare more closely to other test procedures carried out on reversible fuel cells.

Once the overnight activation was complete, an initial IV sweep was imposed on the cell to ensure performance was comparable to previous cells. After this sweep, the cell was voltage was adjusted to the appropriate bias point as described below. For the first test, carried out with the fuel cell in power production mode, the cell was held at a current density of approximately 100mA/cm^2, which for these cells was equivalent to a current of 1.81A, and a corresponding voltage of approximately 550mV. During this test, gas flows remained at 50 sccm of oxygen and 200 sccm of

nitrogen to the cathode and 200 sccm of hydrogen to the anode. For the second test, carried out with the fuel cell in electrolysis mode, the cell current density was held at approximately -100mA/cm^2 with a corresponding voltage of roughly 1.35V. During this test, the gas flows were adjusted to 50 sccm of oxygen and 200 sccm of nitrogen to the cathode and 30 sccm of water vapor and 70 sccm of hydrogen to the anode.

Once the cells were adjusted to the appropriate bias points, an initial EIS sweep was taken over the frequency range 0.1Hz to 10kHz. The sweeps performed here were single 295s logarithmic sweeps covering the entire frequency range, collected with the NI 9206 data acquisition card. The amplitude of the sweep was approximately 25mV and approximately 150mA, though this changed somewhat with frequency. EIS sweeps were then taken two times per day at approximately 10 to 14 hour intervals to provide a means of assessing the change in bias point over time. The final EIS sweep was taken 100 hours after the first sweep. This was followed by a final IV curve to compare to initial behavior. IV curves were not taken during the test so that the cell voltage and current did not vary far from the bias point. At the conclusion of testing, the cells were cooled down by the same procedure performed in the previous experiment discussed in chapter 4.

The first test, in power production mode, revealed some issues with the test stand that were later corrected, but may have affected cell performance. After the cell reached 800°C, it was found that the top platen was not in physical contact with the silver mesh on the cell cathode. This left the cell in perpetual open circuit conditions and prevented any further testing. Once this was observed, the cell was cooled to 600°C, the oven was opened, and a second layer of silver mesh was placed

on the first layer. The oven was closed again and it was found that the additional layer was sufficient to create electrical contact and allow for cell testing. The top alumina felt layer was slightly damaged during this process, but the bottom layer did not appear to be affected. There was concern that this procedure could have caused cell damage due to rapid thermal changes when the oven was opened; however, IV curves did not suggest significant degradation and the test was continued.

In the same test, before the second EIS sweep, the hydrogen flow was diverted through the test tubes with the intent to introduce a small percentage of water vapor to the anode. However, upon redirecting the flow, acoustic noise was heard at the cell which is believed to be indicative of liquid water in the line based on previous experimental observations. The flow was immediately redirected through the bypass valve and held there for the remainder of the test. The fuel cell initially appeared to suffer some degradation from this process, though it later exhibited a degree of recovery.

Finally, the nitrogen tank was switched out during cell operation meaning that for several minutes the cathode was exposed to pure oxygen. However, this is not known to cause degradation as it was similar to the conditions of previous tests. A small change in the bias point was observed after mounting the new nitrogen tank.

Results

Fuel Cell Test

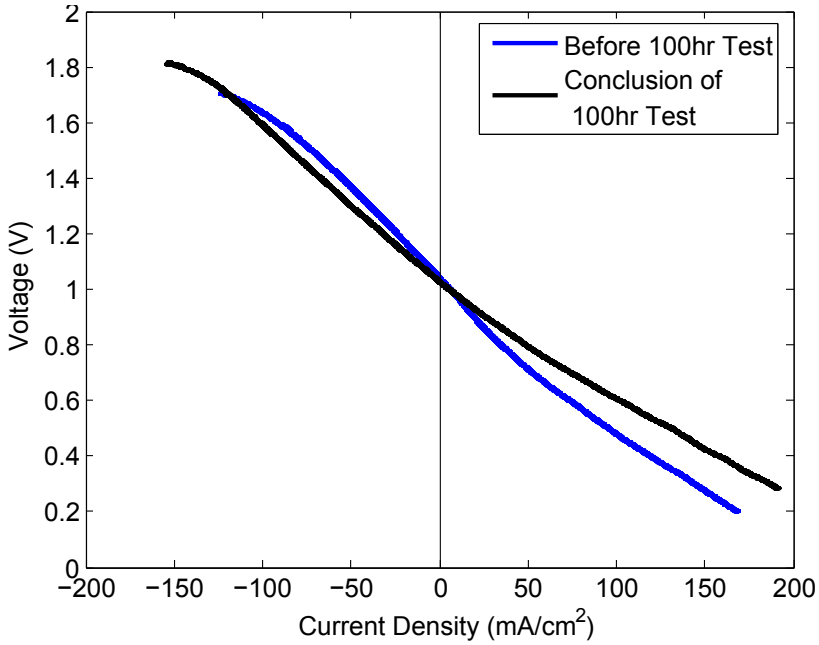

Figure 5.1: Initial and final IV performance of a fuel cell operated at 100mA/cm^2 for 100 hours. The cell shows an overall trend toward improved performance.

IV Data: The initial and final IV curves from the 100 hour fuel cell degradation test are shown in Figure 5.1. From the IV curves, it appears that the cell has improved in performance over the course of the test. The resistance in fuel cell operation was found to decrease from 0.230 Ωcm^2 to 0.197 Ωcm^2, an improvement of 14 percent. This is consistent with observations seen in similar anode supported cell experiments and may be due to a complete reduction of anode NiO to Ni over the course of a longer test.

The modified platens still do not demonstrate perfect sealing as is evident by the passage of negative current. However, the resistance in reverse operation here is approximately 32% higher than that in fuel cell operation. This is a more substantial

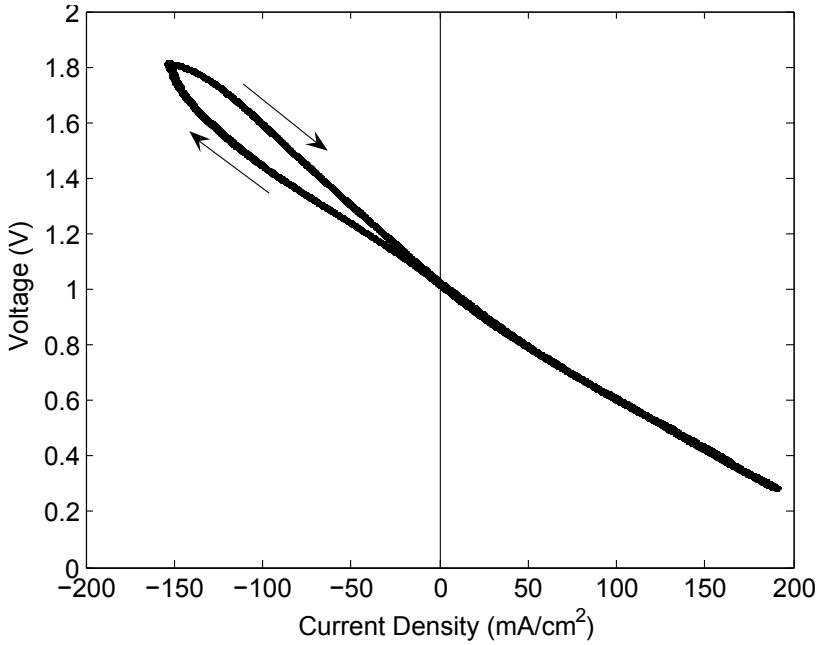

Figure 5.2: Hysteresis in the fuel cell IV curve in the electrolysis region.

increase than seen with the old platens, suggesting that the amount of oxygen leakage has decreased. In addition, dramatic hysteresis is observed in electrolysis mode. This effect is shown in Figure 5.2. Here the fuel cell resistance is lower as the voltage is rising and higher as the voltage is falling. This suggests that at least some of the oxygen on the anode is being transferred to the cathode faster than it is replenished during electrolysis operation. This decreases the partial pressure of oxygen at the anode and leads to increased open circuit voltage and increased electrolysis resistance. The effect of hysteresis appears minimal during fuel cell operation.

EIS Data: The EIS plots obtained during fuel cell operation reveal several important ideas. In Figure 5.4, the plot of the cell response at the beginning of the test

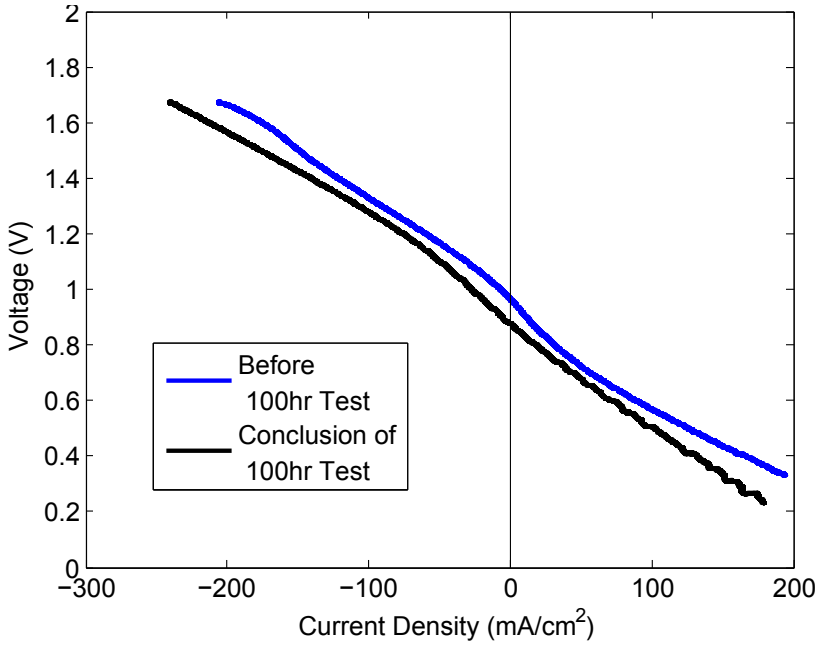

Figure 5.3: Initial and final IV performance of a fuel cell operated at -100mA/cm^2 for 100 hours. The cell shows a drop in open circuit voltage and an increase in resistance in the fuel cell region.

can be compared that at the second sweep after roughly 18 hours under 100mA/cm^2. The cell showed an increase in ionic polarization resistance, an increase in the maximal imaginary resistance, and an increase in series resistance, though an exact value cannot be determined for the last. This shows evidence of decreased performance, which corresponds to the introduction of liquid water to the cell anode as discuss in chapter 5.

From the above observations, it seems that moderate fuel cell operation may cause degradation. However, Figure 5.4 also compares the response after some degradation to the final response after 100 hours at 100mA/cm^2. Here performance appears to

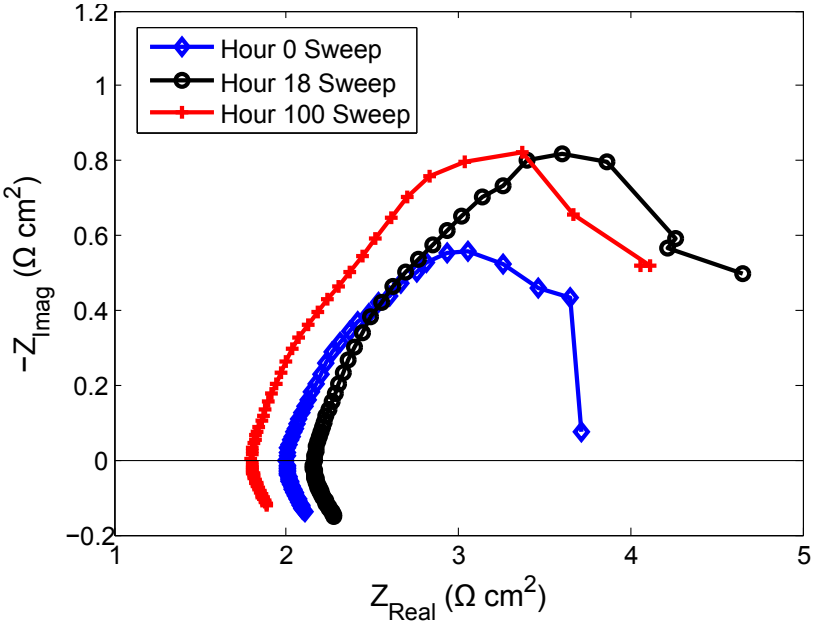

Figure 5.4: Comparison of EIS response at 0 hours, 18 hours, and 100 hours. Initially cell impedance increases substantially. Later the cell shows a significant decrease in ionic polarization resistance, but a small change in series resistance.

have recovered substantially. Ionic polarization resistance decreased to 1.798 Ω cm^2, a drop of 17 percent from the 18 hour sweep. The series resistance, which increased significantly between the first and second sweep, remained relatively constant over the final 80 hours. The precise values are impossible to determine accurately because the cell response does not reach the real axis at the lowest frequency examined. The value of f_m stayed nearly constant over the duration of the test.

A plot of the change in ionic polarization resistance over time is shown in Figure 5.5. This provides some measure of the progression of cell performance over time. Except for the initial spike, believed to be due to the addition of liquid water to the cell, the ionic polarization resistance decreased slightly over time to below the

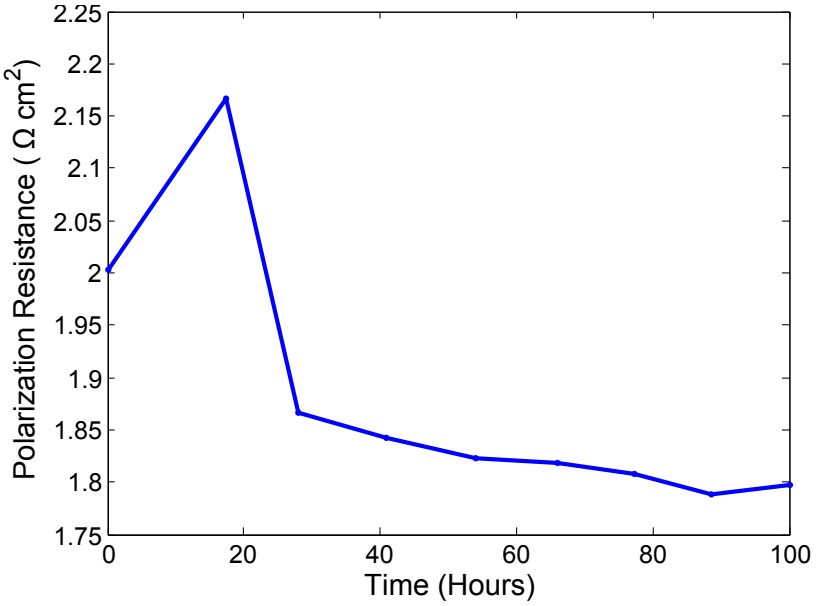

Figure 5.5: Plot of the ionic polarization resistance over the course of the 100 hour test. Except for the spike at the second test point, the ionic polarization resistance shows an overall decrease.

initial level. From this data, it appears the cell has approached a steady state ionic polarization resistance by the end of the 100 hour test.

SEM Imaging: SEM imaging revealed no damage over the majority of the cell operated in fuel cell mode. Several small pits were seen in the anode and electrolyte although these may have been caused by imperfections in cell construction and cannot necessarily be attributed to this test. However, one portion of the cell exhibited significant delamination between the electrolyte and anode. This can be seen in Figure 5.6. While only one instance of delamination was found, this suggests some damage was sustained during operation. It is not certain whether this damage was

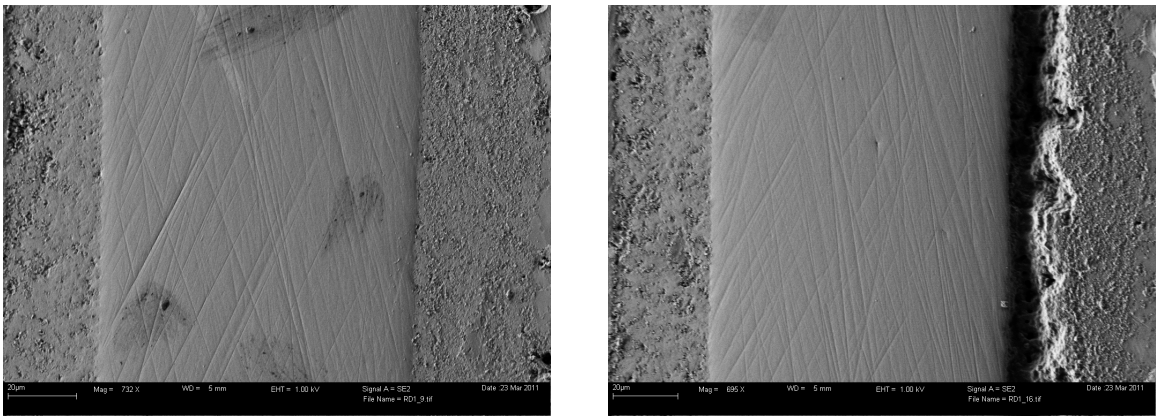

Figure 5.6: SEM images of the fuel cell operated under a positive current. The cell is oriented with the cathode on the left and anode on the right. The left figure is an undamaged portion of the cell for reference and the right figure shows an instance of delamination between the electrolyte and anode.

caused by prolonged operation or by the errors in operation explained in the test procedures section.

Electrolysis Cell Test

IV Data: The initial and final IV curves from the 100 hour electrolysis cell degradation test are shown in Figure 5.3. Here cell degradation is evident. The open circuit voltage decreased by 9.2%, suggesting that cracks have formed in the electrolyte allowing leakage and mixing of hydrogen and oxygen which lowers the actual voltage below the ideal Nernst potential. In addition, resistance in fuel cell operation increased slightly, about 2%, from 0.141 Ωcm^2 to 0.143 Ωcm^2. While resistance in electrolysis mode remained approximately constant at 0.213 Ωcm^2, the overall EVE at 100mA/cm^2 decreased nearly 8%, meaning overall cell performance is worse.

EIS Data: Noise on the cell voltage during electrolysis operation, was sufficient to disrupt low frequency EIS analysis. This bubble noise is a small, but non-negligible effect that occurs primarily between 1 and 10Hz and decreases the reliability of the EIS readings at those frequencies. This creates additional noise on the plots at the low frequency range, preventing a good estimate of series and DC resistances and the frequency of maximal imaginary response. However, many useful characteristics can still be determined from the available data sets.

The Nyquist plots of the impedance response during electrolysis operation are shown in Figure 5.7. Here plots are shown for the initial sweep, the sweep at 58 hours, and the final sweep. This shows that the cell progressed through at least two distinct stages. The shift to the right from the initial sweep to the 58 hour sweep is indicative of cell degradation. However, as time increased beyond roughly 60 hours, the response shifted back to the left, representing a decrease in electrolysis impedance that is suggestive of improved performance.

Once again, the progression can be seen by examining the change in ionic polarization resistance over time. Figure 5.8 shows that the resistance increased initially, began to level out, then decreased until the conclusion of the test. Though the estimated changes in the series resistance were more erratic, the overall trend was an initial increase followed by a progressive decrease. Values for f_m could not be determined accurately due to the effects of bubble noise.

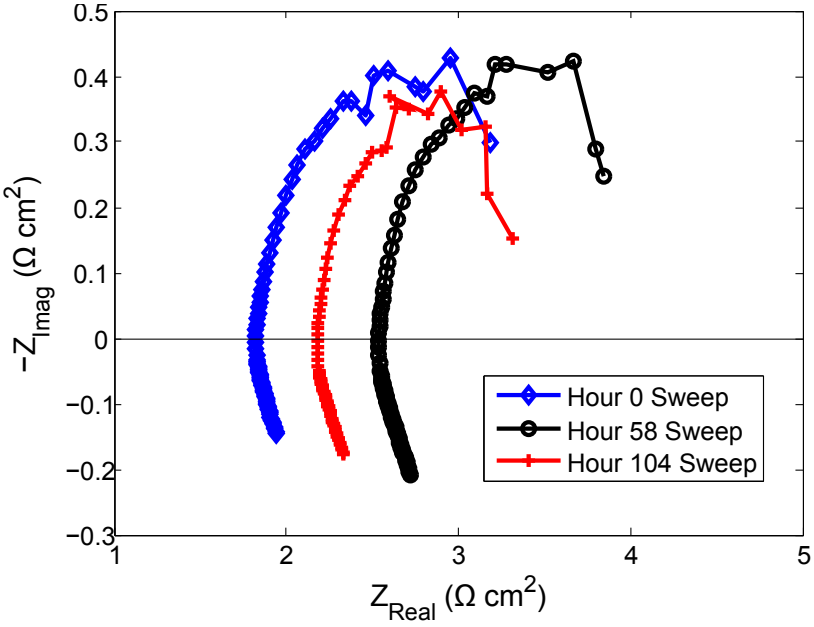

Figure 5.7: EIS response of the electrolysis cell over the course of 100 hours. Initially, the cell impedance increases significantly, but after roughly 60 hours cell impedance decreases.

SEM Imaging: The cell operated in electrolysis mode was found to have minimal damage in the cell microstructure. SEM images do reveal a number of small cracks at the electrolyte and cathode interface. The largest of these cracks has led to delamination at the interface as shown in Figure 5.9. Some of the smaller cracks may mark the beginning of further delamination or they may be cell imperfections. One partial crack was also observed through the electrolyte.

The imaging here suggests that the prolonged operation may lead to delamination between the cathode and electrolyte. This observation is consistent with a number of other studies performed on solid oxide cells run in electrolysis operation [22, 23, 24]. However, the cell was also observed to be highly damaged on a larger, directly visible,

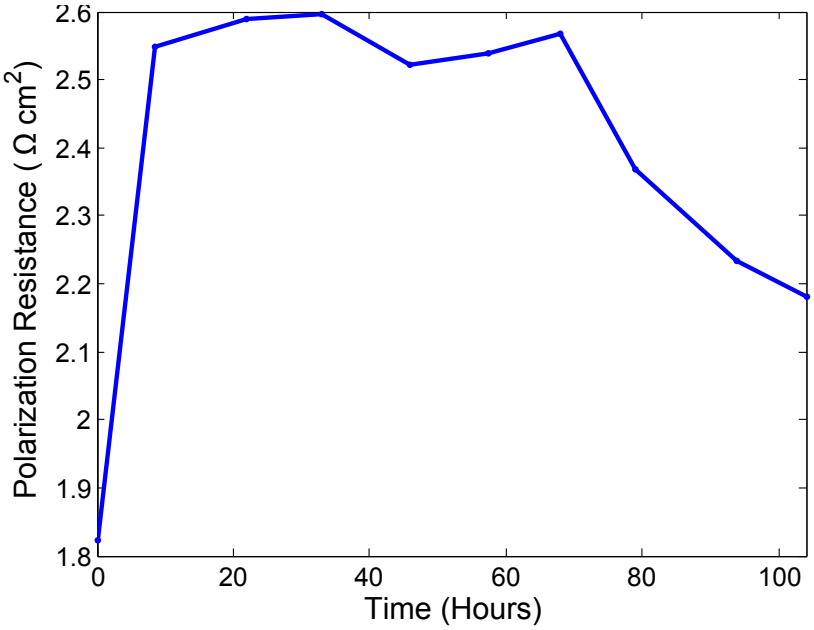

Figure 5.8: Plot of the ionic polarization resistance over the course of the 100 hour test. The resistance initially increases dramatically, then remains relatively stable before decreasing 68 hours into the test.

scale. The cell was fractured into several pieces, similar to the cell observed in the steam variation experiment described in chapter 4. This damage may be due in part to steam exposure or possibly physical stress from high pressure.

Conclusions

Fuel Cell Test

The first fuel cell experiment is difficult to draw conclusions from due to the dramatic cell changes observed 18 hours into the test when water was briefly supplied to the cell. Nevertheless, several observations can be tied together to suggest what

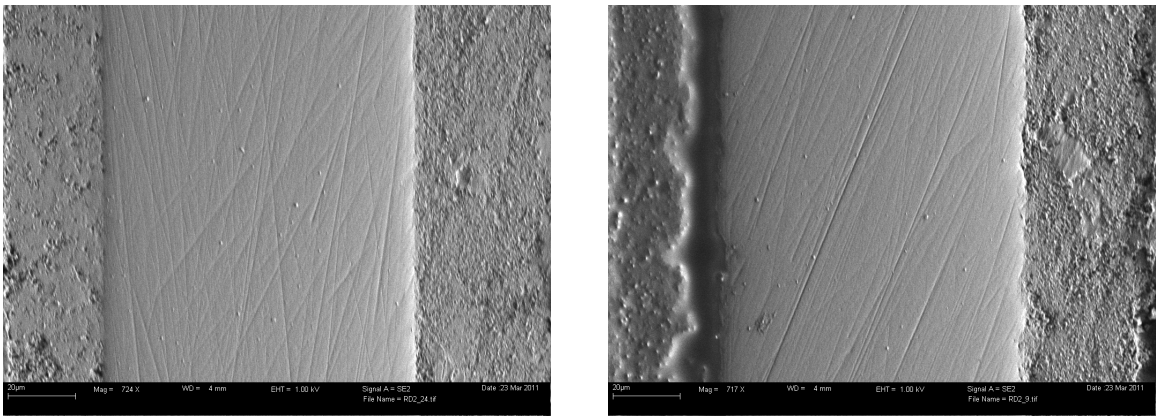

Figure 5.9: SEM images of the fuel cell operated under negative current. The cell is oriented with the cathode on the left and anode on the right. The left figure is an undamaged portion of the cell for reference and the right figure shows delamination between the electrolyte and cathode.

happened to the cell. Figure 5.4 strongly suggests that the brief introduction of water caused cell degradation as evidenced by the increase in both ionic polarization and series resistance. However, from the figure, it is also apparent that the cell recovered to a degree from this damage. The ionic polarization resistance decreased significantly, although the series resistance does not appear to have recovered to the level of initial cell performance.

This suggests that the anode delamination observed in SEM imaging in Figure 5.6 may have occurred around the 18 hour mark. The observed damage likely accounted for the increase in series resistance since the gap created would tend to inhibit the underlying chemical processes, increasing the apparent anode resistance. The delamination represents irreversible cell damage, consistent with the increase in series resistance.

However, the IV data shows a trend toward overall improvement. This is predominantly governed by the overall decrease in ionic polarization resistance observed during the test. Although the series resistance increased, the sum of the two appears to be smaller at the conclusion of the test than at the beginning.

These observations suggest that the fuel cell, when operated under a moderate positive current, tends toward improved performance. The change in ionic polarization resistance in Figure 5.5 slows somewhat over time, possibly approaching a steady state resistance. However, longer duration tests are necessary to observe further changes to the cell impedance.

Electrolysis Test

The electrolysis cell experiment appears to have progressed through three stages. The first stage was brief and consisted of a significant increase in both series and ionic polarization resistance. The second stage lasted approximately 60 hours and showed relatively stable cell performance. The third stage occurred over the last 30 to 40 hours and involved improvement in electrolysis performance as seen through a decrease in both ionic polarization and series resistance.

The first stage may have been predominately due to the leakage of oxygen described in chapter 4. A leak would have caused the cell to have an artificially higher percentage of steam at the anode which would have allowed less resistance to oxygen transport across the electrolyte and therefore a lower ionic polarization resistance. However, if the leakage occurred at a small rate, the amount of additional oxygen would tend to decrease rapidly once negative currents were drawn since oxygen would

be transported across the electrolyte to the cathode. This would have caused an apparent increase in ionic polarization resistance and would also account for the hysteresis observed in Figure 5.2. This effect would only last until the oxygen percentage at the anode reached a steady state value. While the time constant of this effect is unknown, it should tend to be relatively fast, certainly within a few hours as observed here.

The second stage of stability suggests that the cells are capable of sustaining a moderate negative current for a short period of time without significant degradation. This tells us that despite materials designed for fuel cell use, the cell can perform to a degree as an electrolysis cell.

Initially it seems reasonable to conclude that cell performance improved during the third stage where cell impedance in electrolysis operation was found to decrease. However, when all the data is considered, it becomes apparent that reduced impedance does not necessarily mean that overall cell performance was improved. The situation observed here is very similar to that seen in the previous experiment, where cell damage improved the apparent electrolysis performance but significantly worsened in fuel cell performance. The cell cracks, observed upon cell removal, likely began to form between hours 60 and 70 where the ionic polarization resistance began to decrease. This would allow oxygen to leak across the electrolyte and bind to the carrier hydrogen, increasing the apparent steam percentage. This newly formed steam could then take part in electrolysis. However, only the input steam can provide a net hydrogen gain; the artificially formed steam represents only a loss of cell output efficiency. While the impedance is lower, the net rate of hydrogen production, which

is the most important overall measure of electrolysis performance, may have actually been lower once the damage occurred. With no direct measurement of hydrogen output, the actual electrolysis performance remains indeterminate.

The delamination observed in the SEM imaging could have occurred during any of the stages. The partial cathode delamination would have tended to increase the series resistance, though due to the small amount of damage seen, this increase could have been a small effect. This suggests that the damage may have occurred during the first stage of cell operation in which the series resistance increased dramatically. However, the damage may also have been progressive, slowly increasing over time.

Gradual degradation is consistent with damage seen during other solid oxide electrolysis experiments, during which long-term operation led to cathode/electrolyte delamination [22, 23, 24]. This is potentially caused by a buildup of oxygen pressure at the interface due to limited oxygen diffusion rates through the cathode. The increase in pressure causes fractures to form at the boundary between the cathode and electrolyte. Once a defect has formed, it can cause pressure to build up further, increasing the damage done locally. This effect could be slow, but would tend to create a higher degree of delamination as the duration of electrolysis operation increased.

The overall trend of the cell run in electrolysis mode is toward cell degradation and damage. Despite the period of stability, the final IV curves reveal that the performance of the cell has been decreased dramatically. This is particularly evident when noting that the cell EVE decreased during operation. Regardless of whether electrolysis performance truly improved, reversible cell performance was decreased. In

addition, the mechanical damage done to the cell during the test was irreversible and thus these cells do not appear to be well suited for long term electrolysis operation.

Comparison

The initial IV curves from both the fuel cell and electrolysis degradation tests show that the cell used in the fuel cell test began with higher resistance in both modes of operation. The increase is even more significant in electrolysis operation due to the difference in steam input percentages. While some difference in performance is typically seen from cell to cell, this large difference is likely attributable to the erratic conditions applied to the first fuel cell, particularly the oven cooling and heating and the late addition of the second layer of silver mesh. Although it will be desirable to repeat the fuel cell degradation test to minimize cell differences, the experiment reveals that even a cell that was worse initially will tend to improve when run under fuel cell conditions while a cell run in electrolysis conditions tends to degrade.

The SEM images also reveal that the dominant degradation method can vary depending upon the mode of operation. The electrolysis cell showed some cathode delamination, but the fuel cell showed no evidence of cathode damage. Instead, the degradation incurred during fuel cell mode appeared predominantly in anode delamination. This means that both modes of cell failure must be addressed in reversible cell design.

DISCUSSION

The regenerative test stand has been shown to be capable of effectively varying steam input to the fuel cell and varying voltage conditions to allow for IV and EIS sweeps on cells in both fuel cell and electrolysis operation. While some concern still exists regarding oxygen leakage, this does not prevent effective testing of reversible fuel cells. In particular, this test stand is able to readily evaluate the comparative performance in electrolysis and fuel cell mode in order to determine cell suitability for regenerative operation. Degradation during longer tests can also be observed to evaluate the long term performance potential of these cells.

The testing carried out thus far has been performed solely on commercially available electrolyte supported fuel cells. Although these cells are not designed for reversible performance, it is apparent that they are indeed capable of operating in both fuel cell and electrolyzer modes of operation. However, during the 100 hour electrolysis degradation test, these cells were found to degrade, with an 8% drop in EVE and significant mechanical damage. This suggests that although these cells are capable of reversible performance, they are not suitable for long term reversible operation. In addition, the electrolyte supported cell is inherently less efficient than electrode supported cells, prompting interest in the design of symmetrical electrode supported cells for reversible operation [6, 12].

The addition of in-situ EIS to assist in cell evaluation is particularly important because it provides information beyond that reported in many of the currently published reversible and electrolysis cell studies. During the experiments performed in

this thesis, EIS sweeps suggested that cell impedance decreases in electrolysis operation even when the overall cell performance has degraded. This is believed to be attributed to reduced ionic electrolyte impedance due to a decrease in the oxygen concentration gradient and built-in gradient. These improvements would be useful to reversible operation if they could occur without cell degradation and damage. This effect would potentially occur if the partial pressure of oxygen at the cell cathode was reduced by the introduction of high flow rates of an inert gas. This would dramatically lower both the built-in voltage gradient and the oxygen concentration gradient just as desired. The possibility for improved electrolysis performance under an inert gas purge suggests that this may be a useful direction for future research.

The observations during SEM imaging show that cathode/electrolyte delamination can occur during electrolysis operation. This suggests that improved cell durability may require attention not only to different material, but also to the design of the cathode and the cathode/electrolyte interface. If different construction processes can improve the strength of the interface, the extent of delamination could be contained. In addition, the cathode could be altered to allow an easier passage of oxygen gas, potentially reducing pressure that may contribute to delamination. Alternatively, cells could be designed with electrolytes that allow hydrogen, rather than oxygen, to pass as the charge carrier. The mechanical engineering department at Montana State University has been developing this type of proton conducting reversible fuel cell and continues to explore other avenues for cell design. Similar tests to those described here can be performed to determine which new cell designs are the most effective and to help determine what concerns need to be addressed in future design.

This research has contributed to the objectives set by NASA by illustrating mechanisms of cell degradation and focusing further cell design. In addition, the in-situ EIS techniques described in this thesis can be applied not only to a single cell, but to each cell in a small reversible stack to provide simultaneous evaluation of multiple reversible cells. Although this research is focused on space applications, information here contributes to the development of reversible cells for terrestrial use. The same solar and reversible fuel cell hybrid system that will be used in satellites can be used to provide continuous renewable energy on the planet's surface. Reversible cells can also be coupled with wind farms and other energy sources to provide stable power for a variety of uses. The techniques described in this thesis will be valuable in the development of reversible cells for each of these applications.

REFERENCES CITED

[1] Gregor Hoogers, editor. *Fuel Cell Technology Handbook.* CRC Press, 2003.

[2] M. A.Laugton. Fuel cells. *Engineering Science and Education Journal*, pages 7–16, Feb. 2002.

[3] Meng Ni, Michael K. H. Leung, Dennis Y. C. Leung. Technological development of hydrogen production by solid oxide eletrolyzer cell (soec). *International Journal of Hydrogen Energy*, 33:2337–2354, 2008.

[4] A. Hauch, et al. Durability of solid oxide electrolysis cells for hydrogen production. Technical Report Riso-R-1608, Riso National Laboratory, Denmark.

[5] A. Hauch, et al. Stability of solid oxide electrolyser cells. Technical Report Riso-R-1517, Riso National Laboratory, Denmark.

[6] T. L. Cable, J. A. Setlock. Regenerative performance of the nasa symmetrical solid oxide fuel cell., 2011.

[7] Daniel Rosenberg. Analysis of energy storage system based on regenerative fuel cells for spacecraft. *57th International Astronautical Congress*, Oct. 2006.

[8] T. L. Cable, J. A. Setlock. Regenerative operation of the nasa symmetrical support solid oxide fuel cell. *Ceramic Engineering and Science Proceedings*, 28:103–113, 2008.

[9] Craig Nickol, Mark Guynn, Lisa Kohout, Thomas Ozoroski. High altitude long endurance air vehicle analysis of alternatives and technology requirements development. *45th AIAA Aerospace Sciences Meeting*, Jan. 2007.

[10] Asbjorn Strand, Helge Weydahl. Regenerative fuel cell systems for satellites. *8th European Conference on Radiation and its Effects on Components and Systems*, Cap d'Agde, France, 2005.

[11] Alvin Bergen, et al. Development of a dynamic regenerative fuel cell system. *Journal of Power Sources*, 164:624–630, 2007.

[12] C. Stoots, J. O'Brien, T. Cable. Test results from the idaho national laboratory of the nasa bi-supported cell design. *2009 ASME International Mechanical Engineering Congress and Exposition*, pages 1–7, Lake Buena Vista, Florida, USA, Nov. 2009.

[13] A. Momma, et al. Polarization behavior of high temperature solid oxide electrolysis cells (soec). *Journal of the Ceramic Society of Japan*, 105:369–373, 1997.

[14] Bruce Mayer, Craig C. Collins, Mike Walton. Transient analysis of carrier gas saturation in liquid source vapor generators. *Journal of Vacuum Science and Technology*, 19:329–344, 2001.

[15] J. I. Gazzarri, O. Kesler. Electrochemical ac impedance model of a solid oxide fuel cell and its application to diagnosis of multiple degradation mechanisms. *Journal of Power Sources*, 167:100–110, 2007.

[16] J. Ross Macdonald. Impedance spectroscopy. *Annals of Biomedical Engineering*, 20:289–305, 1992.

[17] Qiu-An Huang, et al. A review of ac impedance modeling and validation in sofc diagnosis. *Electrochimica Acta*, 52:8144–8164, 2007.

[18] K. J. Runtz, M. D. Lyster. Fuel cell equivalent circuit models for passive mode testing and dynamic mode design. *IEEE CCECE/CCGEI*, May 2005.

[19] Singaravelu Elangovan, Joseph J. Hartvigsen, Lyman J. Frost. Intermediate temperature reversible fuel cells. *International Journal of Applied Ceramic Technology*, 4:109–118, 2007.

[20] Anil V. Virkar. A model for solid oxide fuel cell (sofc) stack degradation. *Journal of Power Sources*, 172:713–724, 2007.

[21] Meng Ni, Michael K. H. Leung, Dennis Y. C. Leung. Parametric study of solid oxide steam electrolyzer for hydrogen production. *International Journal of Hydrogen Energy*, 32:2305–2313, 2007.

[22] Jie Guan, et al. High performance flexible reversible solid oxide fuel cell. Technical Report, GE Global Research Center, May 2007.

[23] Manohar S. Sohal. Degradation in solid oxide cells during high temperature electrolysis. Technical Report, Idaho National Laboratory, May 2009.

[24] Jennifer R. Mawdsley, et al. Post-test evaluation of oxygen electrodes from solid oxide electrolysis stacks. *International Journal of Hydrogen Energy*, 34:4198–4207, 2009.

[25] David J. Bents, et al. Hydrogen-oxygen pem regenerative fuel cell development at nasa glenn research center. *Fuel Cells Bulletin*, pages 12–14, Jan. 2006.

[26] Huayang Zhu, et al. Modeling elementary heterogeneous chemistry and electrochemistry in solid-oxide fuel cells. *Journal of the Electrochemical Society*, 152:A2427–A2440, 2005.

[27] A. Hauch, et al. Solid oxide electrolysis cells: Microstructure and degradation of the ni/yttra-stabilized zirconia electrode. *Journal of the Electrochemical Society*, 155:B1184–B1193, 2008.

APPENDIX A

TIME-DOMAIN ANALYSIS FOR ELECTROCHEMICAL IMPEDANCE SPECTROSCOPY: BY PETER LINDAHL AND MATTHEW CORNACHIONE

Introduction

Electrochemical impedance spectroscopy (EIS) is often used to characterize the small signal impedance of an electrochemical device, in this case a fuel cell. These impedance measurements are generally taken over a range of frequencies and thus EIS determines the frequency response of the cell. The hope is that determining the impedance of the fuel cell through EIS can provide information about the operating mechanisms of the cell that cannot be obtained from a purely DC analysis.

In performing EIS, a small amplitude signal, often sinusoidal in nature, is typically imposed on the current through or the voltage across the fuel cell. The cell voltage and current responses are then measured and analyzed to produce a measurement of the cell impedance. If the signal has a broad frequency spectrum, or if the imposed signal is swept through a range of frequencies, then the analyzed current and voltage measurements can give the cell impedance as a function of frequency.

$$Z_c(j\omega) = \frac{V_c(j\omega)}{I_c(j\omega)} \tag{A.1}$$

Several methods to performing EIS have been proposed. Most of these methods entail a time-domain to frequency-domain conversion for determining impedance measurements at specific frequencies. These techniques are often susceptible to noise present in the current and voltage measurements and can result in high degrees of uncertainty in the calculated impedance. Conversely, the system described below pro-

vides a time-domain based EIS analysis technique for determining the small signal impedance as a function of frequency.

In applying this technique, we impose a small amplitude sinusoid on top of the fuel cell's DC current. This sinusoid is logarithmically swept in frequency for excitation of the cell over a broad frequency band. The cell voltage and current responses are measured and sinusoidal waveforms are fit to these measurements effectively filtering-out process and measurement noise. Through the application of simple trigonometric identities, amplitude and phase information can be extracted in the time domain from these fit waveforms and used to generate a non-parametric impedance model of the fuel cell as a function of frequency.

Analysis of Measurements

The analysis of the cell voltage and current measurements follows a two-step least-squares fitting process. First, using non-linear least squares (NLLS) techniques, a model of the excitation signal's phase is found. This is an important first step as knowing the phase of the excitation signal allows the use of ordinary least squares (OLS) in fitting sinusoidal waveforms to the voltage and current measurements. Following this, the amplitude and phase information of these waveforms are used to calculate the amplitude and phase of the cell's impedance. Finally, these values are converted into real and imaginary components of the impedance and plotted on a Nyquist plot.

Non-Linear Least Squares (NLLS) Fit of Excitation Phase

The excitation signal is assumed to have the form,

$$s(t) = A\sin(\phi(t)) + C, \tag{A.2}$$

where A is the signal amplitude, C is a DC offset, and $\phi(t)$ is the absolute phase of the signal. For a logarithmically swept sinusoid, the frequency increases exponentially in time allowing a constant ratio of time per frequency decade, i.e.

$$f(t) = f_0\beta^t. \tag{A.3}$$

Here, f_0 is the starting frequency corresponding to t = 0, and β corresponds to the rate of frequency increase ($\beta > 1$) or decrease ($\beta < 1$). Knowing the sweep's starting frequency, its ending frequency f_d and the sweep's duration in seconds d, β is found through the following equation,

$$\beta = \left(\frac{f_d}{f_0}\right)^{(1/d)}. \tag{A.4}$$

The absolute phase $\phi(t)$ is integrally related to the frequency $f(t)$ such that,

$$\phi(t) = 2\pi\int_0^t f(\tau)\mathrm{d}\tau. \tag{A.5}$$

Thus, the absolute phase is given by

$$\phi(t) = 2\pi f_0\frac{\beta^{(t-1)}}{\log\beta} + \phi_0, \tag{A.6}$$

where ϕ_0 is the initial phase of $s(t)$.

In our application, the excitation signal comes from the signal generator and is used by the electronic load or the hybrid-source power management controller to impose the sinusoidal ripple on the current drawn by the load. This signal was measured and fit to the above model using the NLLS MATLAB command *lsqcurvefit()*; solving for the parameter vector,

$$p = (\, f_0 \quad d \quad f_d \quad \phi_0 \quad A \quad C \,). \tag{A.7}$$

Because the signal generator's logarithmic sweep does not perfectly follow the ideal model above, the excitation signal was split into several sections with each section fit individually. This allows a highly accurate fit of the excitation signal (overall coefficient of determination, $R^2 > 0.99$), and therefor a highly accurate estimate of the excitation signal phase $\phi(t)$.

Ordinary Least Squares (OLS) Fit of Voltage and Current

The application of the excitation signal to the current creates a response in the current and voltage such that

$$I(t) = A_i(t)\sin(\phi(t) + \psi_i(t)) + I_{dc}(t), \tag{A.8}$$

and

$$V(t) = A_v(t)\sin(\phi(t) + \psi_v(t)) + V_{dc}(t). \tag{A.9}$$

Here, $A_i(t)$, $A_v(t)$ and $\psi_i(t)$, $\psi_v(t)$ represent the time-varying amplitude and phase terms, respectively. The $I_{dc}(t)$ and $V_{dc}(t)$ terms represents the cell's DC op-

erating points, which are shown as functions of time because the cell's voltage and current can drift slightly during the full frequency sweep.

If the reasonable assumption is made that the amplitude, phase and DC operating point of the current changes slowly and smoothly in time, then for fractions of the total sweep, $I(t)$ can be approximated as

$$I_x(t) = A_{ix,} \sin(\phi(t) + \psi_{i,x}) + I_{dc,x}. \tag{A.10}$$

The x index corresponds to a particular fraction of the total sweep, which is split into m sections of equal length.

The time domain fitting of equation A.10 initially appears to be a difficult nonlinear fit due to $\phi(t)$ and $\psi_{i,x}$ both lying inside the argument of the sinusoid. However, using the trigonometric angle summation identity allows the separation of the two so that,

$$I_x(t) = q_{i1,x} \sin(\phi(t)) + q_{i2,x} \cos(\phi(t)) + q_{i3,x}, \tag{A.11}$$

where $q_{i1,x} = A_{i,x} \cos(\psi_{i,x})$, $q_{i2} = A_{i,x} \sin(\psi_{i,x})$, and $q_{i3,x} = I_{dc,x}$. Now, with the phase model extracted from the excitation signal (section A), equation A.11 can be solved for the q parameters using ordinary least squares (OLS).

Similarly, the fuel cell's voltage response to the excitation current can be written as,

$$V_x(t) = q_{v1,x} \sin(\phi(t)) + q_{v2,x} \cos(\phi(t)) + q_{v3,x}, \tag{A.12}$$

where the individual q parameters have analogous meanings to those of the current. They too are found using OLS techniques.

These q parameters are important because they allow the representation of the small signal current and voltage as phase vectors in a Euclidean reference frame, i.e.

$$\vec{I}_x = \begin{bmatrix} q_{i1,x} \\ q_{i2,x} \end{bmatrix}, \tag{A.13}$$

and

$$\vec{V}_x = \begin{bmatrix} q_{v1,x} \\ q_{v2,x} \end{bmatrix}. \tag{A.14}$$

Figure A.1 shows a diagram of these phasors. The small signal impedance of the cell can be thought of as the scaling / rotation matrix that maps the current vector $\vec{I}_x$ onto the voltage vector $\vec{V}_x$ such that,

$$\vec{V}_x = \begin{bmatrix} Z_{real,x} & -Z_{imag,x} \\ Z_{imag,x} & Z_{real,x} \end{bmatrix} \vec{I}_x. \tag{A.15}$$

From the frequency model of the excitation signal $f(t)$ detailed in section A, estimates of the excitation signal frequency can be found for each division of data, x. For each division, the associated frequency is well approximated by the mean frequency,

$$f_x = \frac{\sum_{t=t_1}^{t_n} f(t)}{t_n - t_1}, \tag{A.16}$$

where t_1 and t_n are the time vector value extremes for data division x.

Thus, we have an approximation of the cell's small signal impedance as a function of frequency (equation A.1),

$$Z(j\omega) = Z_{real,x} + jZ_{imag,x}, \tag{A.17}$$

where $\omega = 2\pi f_x$.

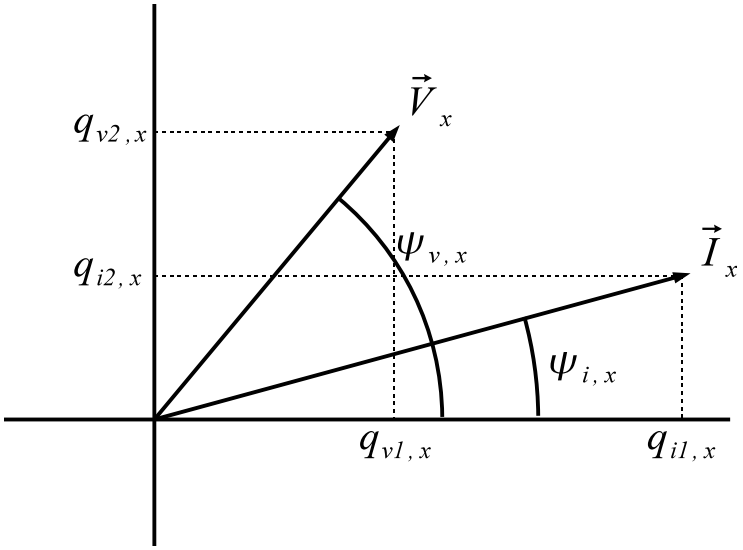

Figure A.1: Phasor representation of the ordinary least squares (OLS) fit voltage and current measurements.

Phase Model Adjustment for Sequential Sampling of Data Acquisition Device

Many data acquisition devices (DAQ) perform sequential sampling of the DAQ's channels. That is, instead of sampling each channel simultaneously, the DAQ channels are sampled sequentially, with a small time delay between samples corresponding to the DAQ's aggregate sample rate. This time delay presents itself as a phase shift in the impedance calculations which grows in size as the frequency content of the excitation signal nears the inverse of DAQ's sample time delay between the current channel and the voltage channel. To compensate for this, a phase shift of equal magnitude can be pre-imposed on the phase model used by the voltage measurement fit. This phase shift is given by,

$$\Delta\phi(t) = 2\pi T_d f(t), \tag{A.18}$$

where T_d is the time delay between the sampling of the current channel and the sampling of the voltage channel.

Practical Considerations

The appropriate number of sweep divisions requires some discretion. If too few divisions are used then the estimates on the current and voltage amplitudes will encompass data with a wide range of frequency excitation. This would violate the assumption made in equations A.11 and A.12 and would give useless single estimates of impedance over a wide range of frequencies. However, if too many divisions are used then the individual fits will tend to be worse as there is less data available for each division's fit and so the accuracy of the impedance estimates can diminish. For our frequency sweeps, we have found that splitting the data into roughly 10 divisions per decade of frequency gives a useful picture of the impedance.